

A numerical analysis of zero-dimensional Fabry-Pérot micro-cavities

Bachelor Thesis

Submission of Bachelor Thesis to the Department of Information Technology and Electrical
Engineering at Swiss Federal Institute of Technology Zürich

Submitted by:

Klemens Flöge

19-953-066

Advisors: Deepankur Thureja
 Dr. Puneet Murthy

Zürich, 03.01.2022

Abstract

Recent advancements in the production of general hexagonal Boron Nitrate (hBN) freeforms on microscopic scales allow for their introduction into micro-cavities to manipulate the electric field distribution within them. The flexibility of creating arbitrary shapes of hBN could result in a new generation of optical micro-cavities. As this procedure was still relatively new at the beginning of the project it was not yet clear what shapes would lead to which electric field distributions. The goal of this project was to build numerical models, which could simulate hBN lens shapes inside Fabry-Pérot cavities and analyse the corresponding electric field distributions. At first a simulation software was used to first replicate existing models of plane-parallel Fabry-Pérot cavities. The further analysis build a number of models to examine the resulting electric field distributions from different curvatures of a single hBN lens and multiple lenses that were introduced to a plane-parallel Fabry-Pérot cavity. A variety of interesting features in the resulting distributions could be found, such as the dependence of the transverse confinement on the curvature of the lens. The behaviour of the system through the introduction of multiple lenses could also be analysed. In conclusion the existing models can be used to model simple lenses of hexagonal Boron Nitrate inside plane-parallel Fabry-Pérot cavities and allow researchers to start investigating more arbitrary shapes and forms.

Contents

1	Introduction	1
2	Theory on optical micro-cavities	3
2.1	Basics of electromagnetic fields	3
2.1.1	Plane Waves	7
2.2	Gaussian beams	7
2.3	Fabry-Pérot Cavities	11
2.4	Distributed Bragg Reflectors	17
2.5	Photon Confinement	22
3	COMSOL Multiphysics®	27
3.1	Theory on Finite Element Method (FEM)	27
3.2	Building a 2D DBR cavity in COMSOL	28
4	Results	37
4.1	2D DBR cavity model without hBN lens	37
4.2	Zero dimensional DBR cavities with one hBN lens	40
4.2.1	Introduction of the hBN lens	42
4.2.2	Dependence of photon confinement on curvature of lens	48
4.2.3	Rayleigh length of Gaussian beams	52
4.3	Zero dimensional DBR cavities with multiple hBN lenses	54
4.3.1	Two lens Model	54
4.3.2	Four lens Model	56
5	Conclusion and Outlook	59
	Bibliography	61
	List of Figures	64
	Appendices	67
A	Appendix: Python code	67

1 Introduction

Fabry-Pérot Cavities are optical devices which consist of two plane-parallel mirrors. These are of great importance to modern optics and a key enabling technology to quantum science. Nanophotonics is the study of the electromagnetic field in dielectric materials on scales comparable to its wavelength. Cavities are a key experimental tool in this research discipline, as they allow the trapping and manipulation of light on microscopic scales by creating resonant modes, which are localised in the cavity. This is especially interesting in the analysis of nanoscale objects such as quantum dots. The effects of placing a quantum dot in a general electromagnetic field are usually quite insignificant. However, "for a smaller and smaller cavity, these resonant modes couple more and more strongly to a single nanoscale object inside it." [11]. It is therefore important for researchers in nanophotonics to understand how the electromagnetic field can be manipulated inside a micro-cavity. The modification of an hexagonal Boron Nitrate (hBN) profile inside the cavity changes the spatial distribution of the relative permittivity, which in turn changes the distribution of the electromagnetic field inside the cavity.

Plane-parallel Fabry-Pérot cavities create a longitudinal confinement of the electromagnetic field. The longitudinal confinement reduces the dimensions of free movement for the photons from three to two. Thus plane-parallel Fabry-Pérot cavities are also referred to as two dimensional cavities. In order to manipulate the photon field further transverse confinement is introduced. If the transverse confinement 'restricts' the movement of photons in both directions in the transverse plane the number of free movement dimensions is effectively reduced to zero. This would then be referred to as a *zero-dimensional Fabry-Pérot cavity* and will be the setup studied in this project. The starting point for this analysis was the development of new production method for hexagonal Boron nitrate freeforms on microscopic scales [27]. Using this new fabrication technique allows for the spatial modulation of the effective refractive index inside the cavity, which gives much greater command on the electric field distribution as will be shown in this analysis. This approach to manipulating the electromagnetic field inside a Fabry-Pérot cavity is much more flexible than existing methods, such as plane-concave Fabry-Pérot cavities. A key difference is that existing methods change the curvature of one or both of the mirrors, which gives the setup two tuning parameters for the transverse confinement. The new hBN freeform method allows for arbitrary shapes to be created which gives scientists much more flexibility in designing

a desired electromagnetic field distribution within the cavity.

This project is meant to provide a starting ground for researchers, who wish to place different shapes and forms of hBN inside a Fabry-Pérot cavity to study their optical behaviour. The main goals of this analysis will be to use the COMSOL Multiphysics[®] simulation software to first replicate existing models of Fabry-Pérot cavities. In a next step an hBN lens will be introduced to the system to study its effect on the electric field distribution and replicate some of the experimental data gathered by researchers. In a final step multiple hBN lenses are introduced to investigate their interference and start off the analysis of general freeform hBN structures in Fabry-Pérot cavities.

This bachelor thesis was completed in the Quantum Photonics Group, Department of Physics at the Swiss Federal Institute of Technology Zürich. The academic advisors were Deepankur Thureja and Dr. Puneet Murthy while the supervision was done jointly by Prof. Dr. Atac Imamoglu and Prof. Dr. Klaus Ensslin

2 Theory on optical micro-cavities

In this chapter some of the basics in electromagnetic theory, Fabry-Pérot cavities and photon confinement will be discussed. The aim of this project was to build numerical simulations for new types of zero dimensional cavities. The experimental data to verify most of the numerical models is yet to be recorded, thus discussing the theory behind the simulations is all the more important. Readers who are more familiar with electromagnetic fields may feel free to skip the section 2.1.

2.1 Basics of electromagnetic fields

In order to understand how the electromagnetic field can be manipulated inside a Fabry-Pérot cavity a few key concepts of electromagnetic fields in general are reviewed in this section. Their behaviour is governed by equations written first in rigorous mathematical form by James Clerk Maxwell during the 19th century in this groundbreaking paper [5]. The equations were than later compacted into the four equations known today by Oliver Heaviside and others. Here the letters \vec{E} , \vec{H} denote the electric and magnetic fields respectively and \vec{j}_{free} the electric current density. Maxwell' equations [25]:

$$\nabla \times \vec{H} = \vec{j}_{free} + \frac{\partial \vec{D}}{\partial t} \quad (2.1)$$

$$\nabla \times \vec{E} = -\frac{\partial \vec{B}}{\partial t} \quad (2.2)$$

$$\nabla \cdot \vec{D} = \rho_{free} \quad (2.3)$$

$$\nabla \cdot \vec{B} = 0 \quad (2.4)$$

The electric and magnetic field \vec{E} , \vec{H} are related to the electric displacement \vec{D} and magnetic intensity \vec{B} through the following constitutive relations:

$$\vec{D}(r, t) = \epsilon \vec{E}(r, t) \quad (2.5)$$

$$\vec{B}(r, t) = \mu \vec{H}(r, t) \quad (2.6)$$

Where ϵ is the electric permittivity and μ the magnetic permeability. The following assumptions and their justification underlie the equations above and the analysis of the cavities in this project. These were taken from [26]:

- *Isotropic medium*: The electric permittivity and magnetic permeability are identical in all directions of the medium, leading to the constitutive relations in equations 2.5 and 2.6.
- *Linearity*: Optical non-linearities encountered in the materials considered in this project are small enough to be treated perturbatively.
- *Frequency independence*: The frequency independence of the refractive index n or the electric permittivity ϵ can be justified since the operation of the optical resonators is done in a narrow frequency range where the permittivity is nearly constant.
- *Source free*: The cavity considered does not possess any current injection system, so $\vec{j}_{free} = 0$ in 2.1.

The last assumption was made for the cavities considered in this project. The electric permittivity $\epsilon = \epsilon_0 \epsilon_r$ and magnetic permeability $\mu = \mu_0 \mu_r$ can be written as a product of their value in a vacuum and a material dependent relative component. During this project the relative magnetic permeability was assumed as $\mu_r = 1$. The values of these quantities in a vacuum ϵ_0, μ_0 are fundamental constants in physics. Their values in vacuum in SI units are the following:

$$\mu_0 = 4\pi \times 10^{-7} \text{Hm}^{-1} \quad (2.7)$$

$$\epsilon_0 = \frac{1}{\mu_0 c^2} \quad (2.8)$$

Where c is the speed of light in a vacuum.

In a cavity setup a laser beam propagates through the system. Light in general is described as an electromagnetic wave and thus governed by Maxwell's equations. In order to better understand possible solutions to Maxwell's equations the wave equation will be derived, this derivation was mainly taken from [29]. As listed in the fourth assumption the electric current density $\vec{j}_{free} = 0$ is considered to be zero. The constitutive relations with the respective constants can be substituted in the first equation 2.1 which then takes the

following form.

$$\nabla \times \vec{B} = \frac{1}{c^2} \frac{\partial}{\partial t} \vec{E} \quad (2.9)$$

If the rotation operator is applied to both sides of the equation 2.2:

$$\nabla \times \nabla \times \vec{E} = \nabla \times \left(-\frac{\partial}{\partial t} \vec{B} \right) \quad (2.10)$$

$$\nabla \times \nabla \times \vec{E} = -\frac{\partial}{\partial t} (\nabla \times \vec{B}) \quad (2.11)$$

Equation 2.9 is used to substitute for $\nabla \times \vec{B}$ to obtain:

$$\nabla \times \nabla \times \vec{E} = -\frac{1}{c^2} \frac{\partial^2}{\partial t^2} \vec{E} \quad (2.12)$$

The derivation of the wave equation is almost complete. Finally only an identity from vector calculus is needed. For any differentiable vector field $\vec{v} : U \subset \mathbb{R}^3 \rightarrow \mathbb{R}^3$ the following holds:

$$\nabla \times \nabla \times \vec{v} = \nabla(\nabla \cdot \vec{v}) - \nabla^2 \vec{v} \quad (2.13)$$

If the identity 2.13 is used in 2.12 to obtain the wave equation [36]:

$$\nabla^2 \vec{E} - \frac{1}{c^2} \frac{\partial^2}{\partial t^2} \vec{E} = 0 \quad (2.14)$$

In order to solve this partial differential equation in three dimensional space a standard separation of variables ansatz is used. The electric field vector \vec{E} is separated as follows:

$$\vec{E}(r, t) = \vec{R}(r)T(t) \quad (2.15)$$

Inserting this separation into the wave equation 2.14:

$$\nabla^2 \vec{R}(r)T(t) - \frac{\vec{R}(r)}{c^2} \frac{\partial^2 T(t)}{\partial t^2} = 0 \quad (2.16)$$

Which can also be written as the following through dividing by $\vec{R}(r)T(t)$ and multiplying by c^2 :

$$c^2 \frac{\nabla^2 \vec{R}(r)}{\vec{R}(r)} = \frac{1}{T(t)} \frac{\partial^2 T(t)}{\partial t^2} \quad (2.17)$$

As usual in the separation of variables ansatz to solve partial differential equations, it can be seen that both sides of the equation depend on different variables. This means that both sides need to be constant. That constant is now set to equal $-\omega^2$. As a result two new differential equations are obtained, where the space $\vec{r} = (x, y, z)$ and time t variables are separated:

$$\frac{\partial^2 T(t)}{\partial t^2} + \omega^2 T(t) = 0 \quad (2.18)$$

$$\nabla^2 \vec{R}(r) + \frac{\omega^2}{c^2} \vec{R}(r) = 0 \quad (2.19)$$

The first equation 2.18 is a ordinary linear second order differential equation whose solutions are given by:

$$T(t) = c_1 \cos(\omega t) + c_2 \sin(\omega t) = \text{Re}\{c \exp(-i\omega t)\} \quad (2.20)$$

c_1 and c_2 are real constant whereas c is complex. Substituting this expression into the ansatz 2.15:

$$\vec{E}(r, t) = \vec{R}(r)T(t) = \vec{R}(r)\text{Re}\{c \exp(-i\omega t)\} = \text{Re}\{c \vec{R}(r)\exp(-i\omega t)\} \quad (2.21)$$

Then define the complex field amplitude is defined as $c \cdot \vec{R}(r)$ and written $\vec{E}(r) = c \cdot \vec{R}(r)$. The Electric field vector can then be expressed as:

$$\vec{E}(r, t) = \text{Re}\{\vec{E}(r)\exp(-i\omega t)\} \quad (2.22)$$

If this expression is now inserted into equation 2.19 the *Helmholtz Equation* is obtained.

$$\nabla^2 \vec{E}(r) + k^2 \vec{E}(r) = 0 \quad (2.23)$$

,with $k = \omega/c$ [29].

2.1.1 Plane Waves

A particularly simple solution to the Helmholtz equation 2.23 is the plane wave. Plane waves were important in this project as plane-parallel Fabry-Pérot cavities can be solved numerically very well if the incident light is described by a plane wave. This solution can be obtained by using the following ansatz:

$$\vec{E}(r) = \vec{E}_0(r)e^{\pm i\vec{k}\cdot\vec{r}} = \vec{E}_0(r)e^{\pm i(k_x x + k_y y + k_z z)} \quad (2.24)$$

If this ansatz is substituted into the Helmholtz equation 2.23 the following dispersion relation is obtained:

$$k_x^2 + k_y^2 + k_z^2 = \frac{\omega^2}{c^2} \quad (2.25)$$

The solution is the given by:

$$\vec{E}(r, t) = \text{Re}\{\vec{E}_0 e^{\pm i\vec{k}\cdot\vec{r} - i\omega t}\} \quad (2.26)$$

In order for this to be a rigorous solution to Maxwell equations in free space the electric field needs to be divergence free. $\nabla \cdot \vec{E} = 0$. This restricts the k-vector to be perpendicular to the electric field vector, $\vec{k} \cdot \vec{E}_0 = 0$.

Plane waves are of particular importance to this project as they present the simplest solution to the Helmholtz equation and are used in many modelling techniques.

2.2 Gaussian beams

In Fabry-Pérot cavities a laser beam is shining into the system. The Gaussian beam solution to the Helmholtz equation is a very useful one in describing compact laser beams, which is why they will be discussed here. The models implemented in the later stages of the project all used ideal Gaussian beams.

$$\vec{E}(x', y', 0) = \vec{E}_0 e^{-\frac{x'^2 + y'^2}{\omega_0^2}} \quad (2.27)$$

Here \vec{E}_0 is a constant field vector in the transverse xy-plane. The beam waist is chosen to be at $z = 0$ and its radius is given by ω_0 . Through using some tools from Fourier analysis and the paraxial approximation the full solution $\vec{E}(x, y, z)$ in three dimensional space is obtained. The derivation was not directly relevant to this project and will not be done. Interested readers are referred to any standard introductory text on electromagnetic waves

and fields.

To gain a more intuitive understanding of the parameters involved the variable $\rho^2 = x^2 + y^2$ and parameter z_0 are introduced:

$$z_0 = \frac{k\omega_0^2}{2} \quad (2.28)$$

One obtains the following formula for a Gaussian beam [28].

$$\vec{E}(\rho, z) = \vec{E}_0 \frac{\omega_0}{\omega(z)} e^{-\frac{\rho^2}{\omega^2(z)}} e^{i(kz - \eta(z) + k^2 \rho^2 / 2R(z))} \quad (2.29)$$

Where the following abbreviations were used:

- Beam waist: $\omega(z) = \omega_0(1 + z^2/z_0^2)^{1/2}$
- Wavefront radius: $R(z) = z(1 + z^2/z_0^2)$
- Phase correction: $\eta(z) = \arctan(z/z_0)$

The transverse beam width is commonly defined as the width at which the magnitude of Gaussian field distribution decays to $1/e$ of its peak value.

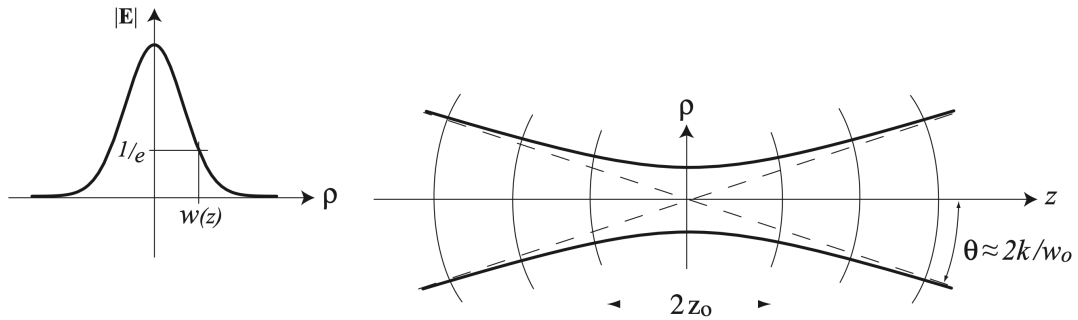


Figure 2.1. Illustration of a Gaussian Beam [28]

The parameter z_0 is also known as the *Rayleigh Length*. Depending on different values for z , three main cases can be distinguished [13].

- $z = 0$. The beam waist is the given by $\omega(z) = \omega_0$. At this point the beam waist attains its minimum, for any $z \neq 0$ the beam waist will be larger. As a result a Gaussian beam's minimal width is always at its focal point.
- When $z = z_0$, the beam waist is given by $\omega(z) = \sqrt{2}\omega_0$. The Rayleigh length marks a turning point for the beam waist radius. For $z < z_0$ the beam waist radius is assumed to be approximately constant. For larger values of z , $z > z_0$ the radius is increasing.

- For $z \gg z_0$ the beam waist radius almost expands linearly. This is indicated in 2.1 with the dashed lines. As the expansion is linear, the beam waist radius can be written as $\omega(z) = \theta z$. The value of θ is given by

$$\theta = \frac{2k}{\omega_0} = \frac{\lambda}{\pi\omega_0}$$

One could conjecture that the Rayleigh length is an arbitrarily chosen value. However there is an intuitive reason for choosing this parameter. At $z = z_0$, $\omega(z) = \sqrt{2}\omega_0$, which means that the cross section of the beam doubled at the Rayleigh length. For $z < z_0$ the ray description of the propagation of light breaks down, as the paraxial approximation is no longer feasible [13]. This means that the Rayleigh length is an important length scale to keep in mind when trying to consider optical systems whose incident electromagnetic waves are Gaussian beams. Some more investigation into the Rayleigh length was done in the later stages of the project which is discussed in section 4.2.3.

In many physical situations it is often advantageous to include energy considerations into the analysis. For this the term intensity will be introduced. In optical physics, the intensity I , e.g. of a laser beam at some location, "is generally understood to be the optical power per unit area, which is transmitted through an imagined surface perpendicular to the propagation direction" [30]. An expression for the intensity of monochromatic waves¹ such as plane waves or Gaussian beams is given by the following:

$$I = \frac{v_p \mu_0 \mu_r}{2} |\vec{E}|^2 = \frac{c \epsilon_0 n}{2} |\vec{E}|^2 \quad (2.30)$$

Taking the Gaussian beam into consideration one can write that the initial intensity I_0 by substituting \vec{E}_0 into the formula above:

$$I_0 = \frac{c \epsilon_0 n}{2} |\vec{E}_0|^2$$

To then obtain a formula for the intensity along the Gaussian beam for given fixed beam waist distribution. The variable z is fixed to a certain value so that the beam waist radius $\omega(z) = \omega$ is constant. Most of the energy resides within the beam waist radius ω , which is what one would expect. The intensity profile in dependence of ρ is then given by the following formula [16].

$$I(\rho) = I_0 e^{-2\rho^2/\omega^2} \quad (2.31)$$

In addition to the fundamental mode discussed above there also exist higher transverse modes. The fundamental Gaussian mode is a solution to the paraxial Helmholtz Equation.

¹A monochromatic wave is a field which oscillates in time at a fixed angular frequency

This partial differential equation is linear, so any combinations of spatial derivatives of the fundamental mode are also solutions to the same differential equation [28]. The two main families of higher order modes are the Hermite-Gaussian and Laguerre-Gaussian modes. The former is typically encountered in rectangular cavity symmetries while the latter can be observed in circular symmetries. This project was mainly concerned with circular symmetries, which were rotation symmetric around the propagation direction of the beam. As a result the Hermite-Gaussian modes will not be analysed further.

Higher order Laguerre-Gaussian modes can be obtained from the following equation as pointed out by Zauderer [37]:

$$\vec{E}_{nm}^L = k^n \omega_0^{2n+m} e^{ikz} \frac{\partial^n}{\partial z^n} \left(\frac{\partial}{\partial x} + i \frac{\partial}{\partial y} \right)^m \left(\vec{E}(x, y, z) e^{-ikz} \right) \quad (2.32)$$

The indices n, m are integers and the tuple (n, m) classifies the Laguerre-Gaussian mode.

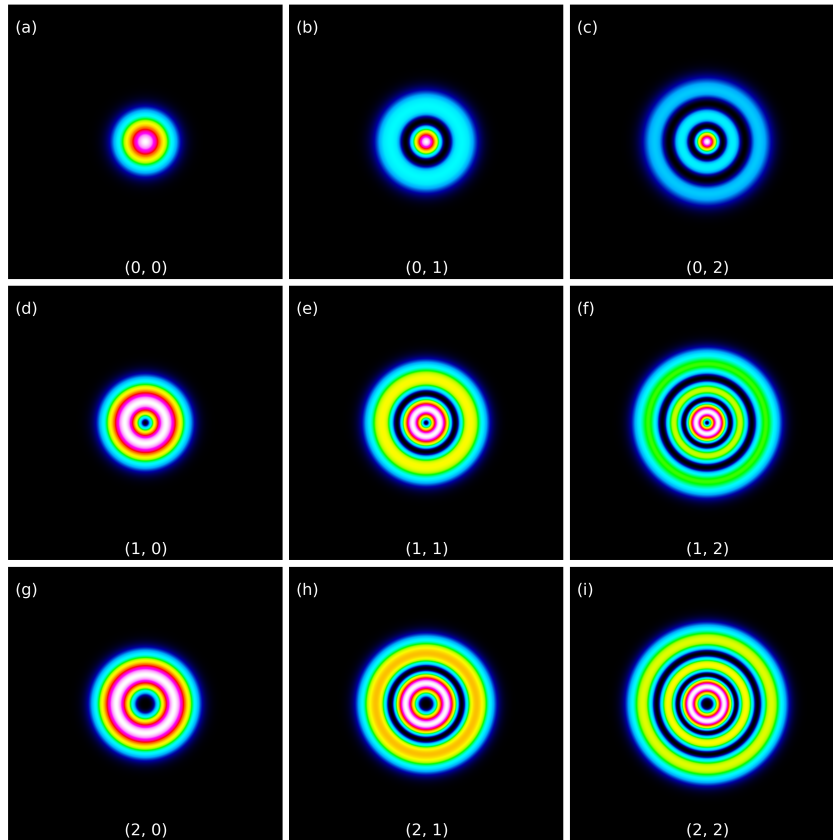


Figure 2.2. A few higher order Laguerre-Gaussian modes [19]

2.3 Fabry-Pérot Cavities

The plane-parallel Fabry-Pérot setup is one of the simplest for realising optical micro-cavities. The setup was invented by the two french physicists Charles Fabry and Alfred Pérot at the end of the 19th century. "A cavity confines the electromagnetic waves in three dimensional space and determines its spectrum through its boundary conditions" [33]. The setup consists of two parallel highly reflective mirrors whose separation can be adjusted. Optical waves can only transit through both mirrors in a resonant mode of the cavity. This is of great relevance as it allows to find resonant modes of the cavity through analysing the transmission spectrum. An illustration of a plane-parallel Fabry-Pérot cavity is given in Figure 2.3.

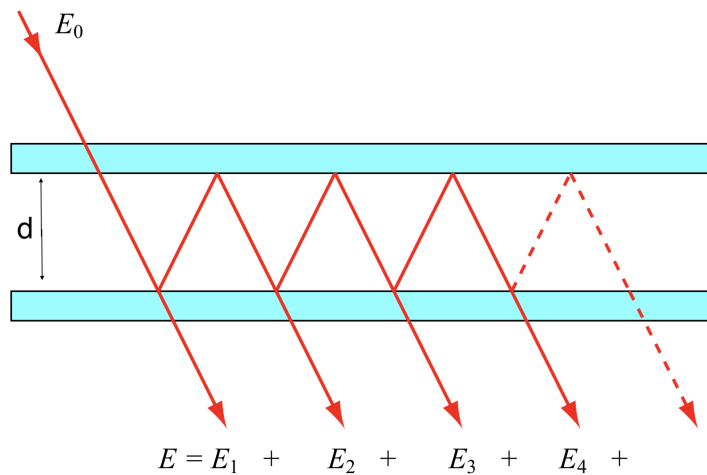


Figure 2.3. A single beam entering the system creates interference of many beams [14]

Depicted in Figure 2.3 is a setup of two highly reflective mirrors at a separation d . Considering the entry of two successive beams to the system at an angle θ , the phase difference between these two beams will be given by the difference in optical path lengths divided by the wavelength and multiplied by 2π :

$$\delta = 2\pi \frac{\Delta \text{Optical Path Length}}{\lambda} = 4\pi d \cos(\theta) \frac{1}{\lambda} = 4\pi d \cos(\theta) \frac{f}{c} \quad (2.33)$$

Where the difference in optical path lengths is given by $2d\cos(\theta)$. The condition for an interference maximum of two coherent beams is that the phase difference is an integer multiple of 2π :

$$\delta = 2\pi m, \text{ with } m \text{ integer} \quad (2.34)$$

Considering two highly reflective mirrors and an incident beam. By introducing the quan-

titles of transmission, reflection and absorption coefficients (T, R and A) one can write the following equation:

$$T + R + A = 1 \quad (2.35)$$

In this analysis the absorption will be assumed negligible, $A = 0$, so 2.35 turns into:

$$T + R = 1 \quad (2.36)$$

If we now assume that on each encounter of the beam with the mirrors a portion of the beam is reflected, as depicted in Figure 2.3. The reflectivity of the mirrors will be denoted as $R = r^2$. The transmission through both mirrors will be written as $T = t^2$. The following expressions for the complex Amplitudes are obtained:

$$\begin{aligned} E_1 &= t^2 E_0 \\ E_2 &= E_1 r^2 e^{-i\delta} \\ E_3 &= E_2 r^2 e^{-i\delta} = E_1 r^4 e^{-i\delta} \end{aligned}$$

The phase difference between two neighbouring waves is written as δ . The 'bouncing' of the beam between the two mirrors as indicated in Figure 2.3 will continue indefinitely with ever decreasing amplitudes. The total amplitude is then given by the infinite summation of all of the individual amplitudes [14]:

$$E = \sum_{i=0}^{\infty} E_i = E_1 \sum_{n=0}^{\infty} r^{2(n-1)} e^{-i\delta n} = \frac{E_1}{1 - r^2 e^{-i\delta}} = t^2 \frac{E_0}{1 - r^2 e^{-i\delta n}} \quad (2.37)$$

The fact that $|R^{2(n-1)} e^{-i\delta n}| = |R^{2n}| < 1$, as $R < 1$ was used to simplify the above series by applying the formula for Geometric Series. Using equation 2.22 the complex electric field vector can be written as:

$$E = t^2 \frac{E_0}{1 - r^2 e^{-i\delta n}} e^{-i\omega t} \quad (2.38)$$

The real valued electric field vector is then obtained by taking the real part of the above expression. In the further analysis of Fabry-Pérot cavity an important parameter to consider are the intensities of the incoming, reflected and transmitted beam. The optical intensity was defined in earlier in equation 2.30. Using this formula and substituting 2.38:

$$I_i = \frac{c\epsilon_0 n}{2} |E_0|^2 \quad (2.39)$$

$$I_t = \frac{c\epsilon_0 n}{2} |E|^2 = \frac{c\epsilon_0 n}{2} |E_0|^2 \frac{t^2}{(1 - r^2 \cos(-\delta))^2 + (r^2 \sin(-\delta))^2} \quad (2.40)$$

Simplifying the latter leads to the following expression.

$$I_t = I_i \frac{t^4}{(1 + r^4) - 2r^2 \cos(\delta)} \quad (2.41)$$

As the absorption is assumed to be zero, $A = 0$, the incident energy flux density should be the same as sum of the energies from the reflected and transmitted waves:

$$I_i = I_r + I_t \quad (2.42)$$

Using $I_r = I_i - I_t$ 2.42 and the trigonometric identity $\cos(\delta) = 1 - 2\sin^2(\delta/2)$ the following equations can be obtained:

$$I_r = I_i \frac{(2r/(1 - r^2))^2 \sin^2(\delta/2)}{1 + (2r/(1 - r^2))^2 \sin^2(\delta/2)} \quad (2.43)$$

$$I_t = I_i \frac{1}{1 + (2r/(1 - r^2))^2 \sin^2(\delta/2)} \quad (2.44)$$

At this point it should be noted that 2.43 can be derived without the assumption in 2.42. In fact the latter can be derived from the former. At this point Hecht's analysis is referred to the interested reader for more details in this derivation [17].

The equation 2.51 can be rewritten in the following forms:

$$\frac{I_t}{I_i} = \frac{T^2}{1 + R^2 - 2R \cos(\delta)} \quad (2.45)$$

$$\frac{I_t}{I_i} = \left(\frac{T}{1 - R} \right)^2 \frac{1}{1 + (4R/(1 - R^2))^2 \sin^2(\delta/2)} \quad (2.46)$$

A maximum in the intensity of the transmitted wave 2.46 will occur if the denominator is as small as possible. Therefore at maximum transmitted intensity one would expect $\sin^2(\delta/2) = 0$, in this case $\delta = 2\pi m$ and

$$(I_t)_{max} = I_i \quad \text{and} \quad (I_r)_{min} = 0$$

By applying the same kind of logic to equation 2.41 the minimum for the transmitted intensity will be attained when $\cos(\theta) = -1$, which is the case for $\delta = (2m + 1)\pi$ and yields the following:

$$(I_t)_{min} = I_i \frac{(1 - r^2)^2}{(1 + r^2)^2} \quad (2.47)$$

$$(I_r)_{max} = I_i \frac{4r^2}{(1 + r^2)^2} \quad (2.48)$$

Examining 2.44 and 2.43 closer it might make sense to introduce a new variable. This quantity is known as the *coefficient of finesse* F and is defined as follows:

$$F = \left(\frac{2r}{1 - r^2} \right)^2 \quad (2.49)$$

The coefficient of finesse can now be substituted in equation 2.44 and 2.43 to obtain:

$$\frac{I_r}{I_i} = \frac{F \sin^2(\delta/2)}{1 + F \sin^2(\delta/2)} \quad (2.50)$$

$$\frac{I_t}{I_i} = \frac{1}{1 + F \sin^2(\delta/2)} \quad (2.51)$$

The term $(1 + F \sin^2(\delta/2))^{-1} = \mathcal{A}(\theta)$ is also known as the *Airy Distribution* [17].

It can be seen in Figure 2.4 that a higher coefficient of finesse leads to sharper peaks in the Airy distribution.

Substitute the definition of the airy distribution and equation 2.51:

$$\frac{I_t}{I_i} = \mathcal{A}(\theta) \quad (2.52)$$

Another quantity of interest which is related to 2.49 is the *Finesse*, which is defined in the following way:

$$\mathcal{F} = \frac{\pi\sqrt{F}}{2} \quad (2.53)$$

To gain a better understanding of the concept of finesse the equation 2.53 is rewritten as

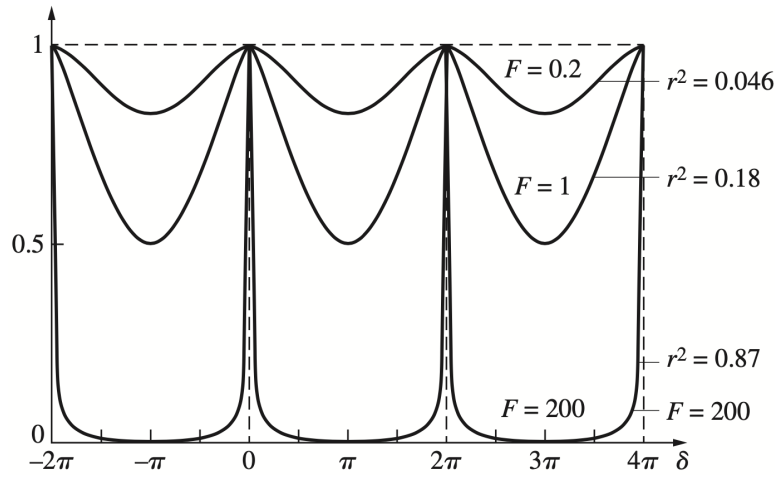


Figure 2.4. Illustration of the Airy function $\mathcal{A}(\theta)$, which plots the ratio of the transmitted intensity I_t to the incident intensity I_i in relation to the phaseshift δ [17]

$F = \frac{4}{\pi^2}\mathcal{F}$ and then substituted into 2.51 to obtain:

$$\frac{I_t}{I_i} = \frac{1}{1 + \frac{4\mathcal{F}^2}{\pi^2} \sin^2(\delta/2)} \quad (2.54)$$

It can now be seen analytically in 2.54 that larger values of the finesse result in sharper peaks in the $\frac{I_t}{I_i}$ vs. δ spectrum. To specify what is meant by 'sharpness' the quantity *Full Width Half Maximum (FWHM)* will be defined. This parameter will be evaluated by determining:

$$\frac{I_t}{I_i} = \frac{1}{2}$$

Using equation 2.54 this condition translates into:

$$\frac{4\mathcal{F}}{\pi^2} \sin^2(\delta/2) = 1 \quad \sin^2(\delta/2) = \frac{\pi^2}{4\mathcal{F}}$$

which results in

$$\sin(\delta/2) = \pm \frac{\pi}{2\mathcal{F}} \quad (2.55)$$

Since the peaks are expected to be rather sharp in a typical cavity the FWHM will be close to the peak. Thus a new parameter ζ will be introduced with $\delta = 2\pi m + \zeta$. Since the FWHM is close to the peak ζ will be small. This can now be substituted into to obtain [35]:

$$\pm \frac{\pi}{2\mathcal{F}} = \sin\left(\pi m + \frac{\zeta}{2}\right) = (-1)^m \sin\left(\frac{\zeta}{2}\right)$$

ζ is then given by

$$\zeta = 2 \arcsin\left(\pm \frac{\pi}{2\mathcal{F}}\right)$$

Expanding the *arcsin* using its Taylor series

$$\zeta = 2 \left(\pm \frac{\pi}{2\mathcal{F}} + \frac{1}{6} \left(\pm \frac{\pi}{2\mathcal{F}}\right)^3 + \frac{3}{8} \left(\pm \frac{\pi}{2\mathcal{F}}\right)^5 + \dots \right)$$

Since ζ is small a linear approximation is adequate and the higher order terms can be neglected, $\zeta = \pm \frac{\pi}{\mathcal{F}}$. The FWHM is then given by $2|\zeta|$ or $\frac{2\pi}{\mathcal{F}}$. From 2.33 it can be seen that the spacing between successive peaks along the δ axis is given by 2π . Taking the ratio between these two quantities results in the finesse.

$$\frac{\text{Distance between two successive peaks}}{\text{FWHM in single peak}} = \frac{2\pi}{\frac{2\pi}{\mathcal{F}}} = \mathcal{F} \quad (2.56)$$

This is the same finesse introduced almost in equation 2.53. Important to note is that a high finesse results in a sharp peak in the $\frac{I_t}{I_i}$ vs. δ plot.

So far the main principles and characteristics of Fabry-Pérot cavities were discussed. In the remaining part of the discussion of these fascinating setups the resonance is considered through its dependency on frequency. Using the equations 2.33 and 2.46 the resonant frequencies can be expressed as follows.

$$f_m = m \frac{c}{2nd} \quad (2.57)$$

Where m is then called the *longitudinal* mode order [1]. The reason for the word longitudinal is that the direction of confinement of the electric field is in parallel to the propagation direction of the beams. This idea will be developed further in the later section 2.5. The equation 2.57 can also be rewritten using the wavelength:

$$\lambda_m = \frac{2nd}{m} \quad (2.58)$$

Similar to the distance between two successive peaks along the phaseshift δ axis one can ask what is that separation of two successive resonant frequencies. This quantity is known

as the *Free Spectral Range (FSR)*

$$\Delta f_{\text{FSR}} = f_{m+1} - f_m = \frac{c}{2nd} \quad (2.59)$$

"Neglecting material dispersion and mirror penetration effects, the FSR is a constant factor over the entire frequency range" [1]. The Finesse can then also be defined using the free spectral range, which presents a nice analogy to 2.53 and 2.56.

$$\mathcal{F} = \frac{\Delta f_{\text{FSR}}}{\text{FWHM at resonance peak}} \quad (2.60)$$

Another important quantity to consider when talking about optical cavities or resonators in general is the *quality Factor* or *Q-factor*. This quantity corresponds to the average number of rounds-trips made by a resonant photon before it leaves the cavity" [1]. For optical cavities it can be expressed as the resonance frequency divided by the free spectral range:

$$Q = \frac{f_{\text{resonance}}}{\Delta f_{\text{FSR}}} \quad (2.61)$$

[31]. One should note that the Q-factor depends on the resonance frequency so this quantity will not be constant over the spectrum of the cavity. Alternatively the Q-factor can also be defined with respect to the frequency. First the free spectral range is defined with respect to the wavelength:

$$\Delta \lambda_{\text{FSR}} = \lambda_m - \lambda_{m+1} = \frac{2nd}{m(m+1)} \quad (2.62)$$

The Q-factor can then also be expressed with respect to the wavelength as follows:

$$Q = \frac{\lambda_{\text{resonance}}}{\Delta \lambda_{\text{FSR}}} \quad (2.63)$$

An illustration of the quantities Free Spectral Range, Full Width Half Maximum and Finesse with respect to a transmission Plot is shown in Figure 2.5.

2.4 Distributed Bragg Reflectors

For the Fabry-Pérot cavities discussed above high reflectivity of the mirrors is desired. In many physical experiments as well as in the simulations employed in this project distributed Bragg reflectors (DBRs) were used as mirrors. A DBR or Bragg mirror is a mirror structure,

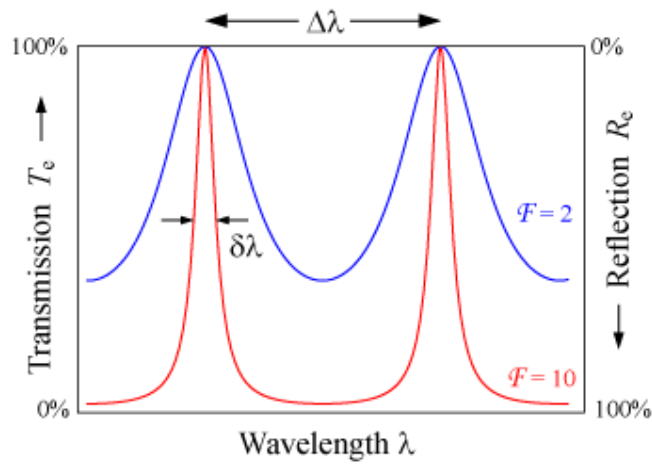


Figure 2.5. Transmission plot of a Fabry-Pérot cavity where the Free Spectral Range, Full Width Half Maximum and Finesse are shown [10]

which consists of repeating layers of two materials with high and low refractive indices respectively. Since the layers alternate in high and low refractive indices, at every other boundary there is a phase shift of π upon reflection from the interface. Hence, the quarter wavelength spacing of the layers is appropriate to give constructive interference in the reflected direction [24]. At vertical incidence the thickness of the high and low refractive index layers $d_{l,h}$ is given by:

$$d_{l,h} = \frac{\lambda_{l,h}}{4} = \frac{\lambda_0}{4n_{l,h}} \quad (2.64)$$

Where n_l and n_h are the low and high refractive indices of the two materials [34] and λ_{ref} is the reference wavelength to which the DBRs are tuned. In this treatment of the DBR mirrors and by extension of the Fabry-Pérot cavities the frequency independence of the refractive indices is assumed. This assumption was made throughout the entirety of the project and in all theoretical derivations as well as numerical models, as explained in subsection 2.1. Typically only a relatively small wavelength range around the the reference wavelength λ_{ref} is considered in order to make the assumption more viable.

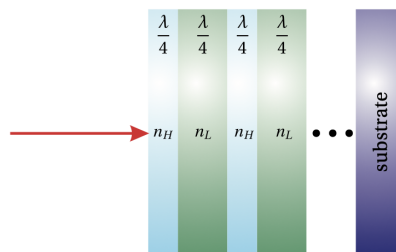


Figure 2.6. Illustration of a distributed Bragg reflector with a quarter wavelength separation of the layers [24]

One of "the most general method of calculating the reflectance R of a multi-layer is based on the matrix formulation of the boundary conditions at the films surfaces" [21]. Following Byrnes [3] in the analysis of the DBR using the transfer matrix method. One considers an incident normal ray of light passing through the stack. The stack is modelled as N layers of thickness d_i and refractive index n_i . The first and last layers will be air, so $n_0 = n_{N+1} = 1$.

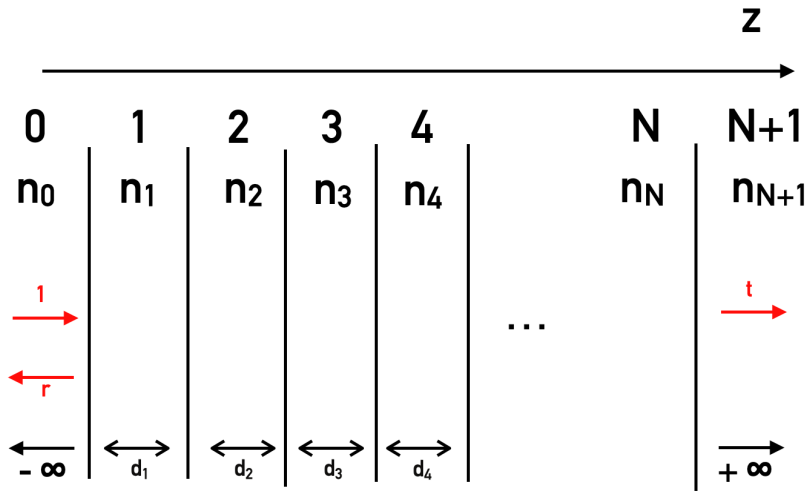


Figure 2.7. A simplified model of a multi-layer stack with N layers where each layer i has refractive index n_i and thickness d_i .

At each point inside the stack the electric field consists of a forward and backward propagating component. The incident beam will be approximated as a plane wave with a electric wave vector in the xz -plane. Equation 2.24 can be used to obtain the general equation for the complex electric field vector

$$\vec{E}(r) = \vec{E}_f e^{i\vec{k}_f \cdot \vec{r}} + \vec{E}_b e^{i\vec{k}_b \cdot \vec{r}}$$

The subscript f indicates the forward propagating part of the beam, while the subscript b references the backwards travelling part. The wave vector \vec{k} is then chosen to be embedded inside the xz -plane.

$$\vec{k}_f = \frac{2\pi n}{\lambda_{vacuum}} \begin{pmatrix} \sin(\theta) \\ 0 \\ \cos(\theta) \end{pmatrix}, \quad \vec{k}_b = \frac{2\pi n}{\lambda_{vacuum}} \begin{pmatrix} \sin(\theta) \\ 0 \\ -\cos(\theta) \end{pmatrix}$$

Considering the interface between the i th and $i + 1$ th layer. From Fresnel's equations [16] the reflectance and transmission coefficients $r_{i,i+1}$, $t_{i,i+1}$ for the interface can be obtained. The following relations between the backward and forward travelling portions of the electric

field of the two layers can be found:

$$\vec{E}_{b,i} = \vec{E}_{b,i+1} t_{i+1,i} + \vec{E}_{f,i} r_{i,i+1} \quad (2.65)$$

$$\vec{E}_{f,i+1} = \vec{E}_{f,i} t_{i,i+1} + \vec{E}_{b,i+1} r_{i+1,i} \quad (2.66)$$

Within each of these layers a phaseshift of $\delta_i = 2\pi d_i n_i / \lambda$ occurs. To simplify the notation, scalar amplitudes are introduced where v_i denotes the forward travelling portion of the wave in the i th layer and w_i the backward part. In addition to this $v_0 = 1$ is the incoming beam, $w_0 = r$ the overall reflection and $v_{n+1} = t$ is the transmission. As only one incident beam from the left is considered, the backwards component behind the stack is zero, $w_{n+1} = 0$.

$$v_{i+1} = v_i e^{i\delta_i} t_{i,i+1} + w_{i+1} r_{i,i+1} \quad (2.67)$$

$$w_i e^{-i\delta_i} = v_i e^{i\delta_i} r_{i,i+1} + w_{i+1} t_{i+1,i} \quad (2.68)$$

Sorting this for v_i and w_i the following are obtained:

$$v_i = v_{i+1} e^{-i\delta_i} \frac{1}{t_{i,i+1}} - w_{i+1} \frac{r_{i+1,i} e^{-i\delta_i}}{t_{i,i+1}} \quad (2.69)$$

$$w_i = v_{i+1} e^{i\delta_i} \frac{r_{i,i+1}}{t_{i,i+1}} + w_{i+1} e^{i\delta_i} \left(t_{i+1,i} - \frac{r_{i,i+1} r_{i+1,i}}{t_{i,i+1}} \right) \quad (2.70)$$

This can now be rewritten more compactly:

$$\begin{pmatrix} v_i \\ w_i \end{pmatrix} = M_i \begin{pmatrix} v_{i+1} \\ w_{i+1} \end{pmatrix} \quad \text{with} \quad M_i = \begin{pmatrix} e^{-i\delta_i} & 0 \\ 0 & e^{i\delta_i} \end{pmatrix} \begin{pmatrix} 1 & r_{i,i+1} \\ r_{i,i+1} & 1 \end{pmatrix} \frac{1}{t_{i,i+1}} \quad (2.71)$$

Combining all of these together with the boundary conditions yields an expression for the transmission and reflection coefficients. The overall characteristic matrix for the multi-layer stack is defined as the product of all the individual layer characteristic.

$$\begin{pmatrix} 1 \\ r \end{pmatrix} = M \begin{pmatrix} t \\ 0 \end{pmatrix} \quad \text{with} \quad M = \frac{1}{t_{0,1}} \begin{pmatrix} 1 & r_{0,1} \\ r_{0,1} & 1 \end{pmatrix} M_1 M_2 M_3 \cdots M_N = \begin{pmatrix} M_{00} & M_{10} \\ M_{01} & M_{11} \end{pmatrix}$$

The reflection coefficients is then given by:

$$r = \frac{M_{10}}{M_{00}} \quad t = \frac{1}{M_{00}} \quad (2.72)$$

With the reflection and transmission coefficients ($R = r^2$ and $T = t^2$) everything of interest in the multi-layer stack can be calculated. This has shown that using the transfer matrix method it is possible to model a DBR mirror for incoming plane waves. The distributed Bragg reflector is tuned to a specific frequency, which involves the quarter wavelength stacks discussed above. Within this regime the mirror is highly reflective. However if much lower or higher frequencies than the tuning frequency are shine onto the stack the reflectance become much smaller.

Over the course of this project the analytical calculations for the DBRs mirrors were not performed. This theoretical discussion served to show the underlying mathematics of a numerical model which simulates DBR mirrors. The analysis done above can be implemented in any high level programming language. In order to verify early models build with COMSOL one of these implementation in Python the so called *TMM* library was used. In Figure 2.8 the transmission spectrum of a DBR as calculated by the python TMM library is depicted.

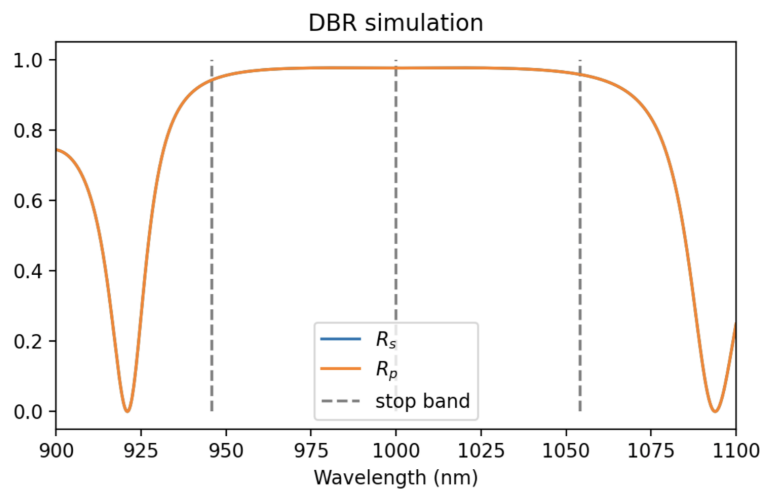


Figure 2.8. Simulation of distributed Bragg reflector of a typical Reflectance vs. Wavelength plot done using the Python TMM library. This plot describes a DBR with 15 Bragg pairs where the refractive indices 2.91 and 3.45 corresponding to the material AIAs and GaAs respectively were used

2.5 Photon Confinement

The theory discussed so far has been about planar or two-dimensional cavities. The photons inside are confined in the longitudinal direction by the two parallel highly reflective mirrors of the plane-parallel Fabry-Pérot cavity. They are still free to move in the two dimensional xy -plane parallel to these two mirrors. In many applications of quantum optics or solid state physics in general one might wish to confine the photons even further. This can be done through introducing 'barriers' inside the cavity in the xy -plane to restrict the movement of the photons. This then corresponds to a reduction of the dimension. If these 'barriers' or materials of higher dielectric constant than the air in the cavity are introduced in both direction of the transverse plane the dimension is reduced to zero.

In order to illustrate the main idea behind photon confinement a key formula will be deduced from Maxwell's equations.

By inserting $\vec{j}_{free} = 0$ and 2.5 into 2.1 the following equation is obtained:

$$\nabla \times \vec{H}(r, t) = \frac{\partial}{\partial t} (\epsilon_0 \epsilon(r) \vec{E}(r, t))$$

Here is noted that the permittivity is written as $\epsilon = \epsilon_0 \epsilon(r)$ to highlight its spatial dependence, as the permittivity varies considerably throughout the cavity. This expression can be rewritten as follows:

$$\begin{aligned} \frac{1}{\epsilon(r)} \nabla \times \vec{H}(r, t) &= \epsilon_0 \frac{\partial}{\partial t} \vec{E}(r, t) \\ \nabla \times \left(\frac{1}{\epsilon(r)} \nabla \times \vec{H}(r, t) \right) &= \epsilon_0 \nabla \times \left(\frac{\partial}{\partial t} \vec{E}(r, t) \right) \\ \nabla \times \left(\frac{1}{\epsilon(r)} \nabla \times \vec{H}(r, t) \right) &= \epsilon_0 \frac{\partial}{\partial t} (\nabla \times \vec{E}(r, t)) \end{aligned}$$

Using the equations 2.2 and 2.6 leads to:

$$\begin{aligned} \nabla \times \left(\frac{1}{\epsilon(r)} \nabla \times \vec{H}(r, t) \right) &= \epsilon_0 \frac{\partial}{\partial t} \left(-\frac{\partial}{\partial t} \vec{B}(r, t) \right) \\ \nabla \times \left(\frac{1}{\epsilon(r)} \nabla \times \vec{H}(r, t) \right) &= -\epsilon_0 \frac{\partial^2}{\partial t^2} (\mu_0 \vec{H}(r, t)) \end{aligned}$$

Through considering monochromatic solutions 2.22 further rearrangements can be made:

$$\begin{aligned}\nabla \times \left(\frac{1}{\epsilon(r)} \nabla \times \vec{H}(r) e^{-i\omega t} \right) &= -\epsilon_0 \mu_0 \frac{\partial^2}{\partial t^2} \left(\vec{H}(r) e^{-i\omega t} \right) \\ \nabla \times \left(\frac{1}{\epsilon(r)} \nabla \times \vec{H}(r) e^{-i\omega t} \right) &= \epsilon_0 \mu_0 \omega^2 \vec{H}(r) e^{-i\omega t} \\ \nabla \times \left(\frac{1}{\epsilon(r)} \nabla \times \vec{H}(r) \right) &= \epsilon_0 \mu_0 \omega^2 \vec{H}(r)\end{aligned}$$

Substituting the relation $c^2 = 1/\mu_0\epsilon_0$ for the speed of light in a vacuum finally yields:

$$\nabla \times \left(\frac{1}{\epsilon(r)} \nabla \times \vec{H} \right) = \left(\frac{\omega}{c} \right)^2 \vec{H} \quad (2.73)$$

$$\Theta \vec{H} = \left(\frac{\omega}{c} \right)^2 \vec{H} \quad (2.74)$$

With the Θ operator being defined as follows:

$$\Theta = \nabla \times \left(\frac{1}{\epsilon(r)} \nabla \times \right)$$

,which has eigenvalues ω^2/c^2 .

The equation 2.73 is sometimes referred to as the *Master's equation* and it captures "the heart of Maxwell's equations for a harmonic mode in mixed dielectric medium" [22]. ²The relative permittivity $\epsilon(r)$ is intricately linked to the refractive index n_i of the different materials in the cavity. This link is given by $n(r) = \sqrt{\epsilon(r)\mu_r} = \sqrt{\epsilon(r)}$ since $\mu_r = 1$. One cannot help but draw a connection to the wave mechanics formalism of quantum theory. The introduction of dielectric materials changes the potential for the photons and thus the magnetic and electric field distributions $\vec{E}(r), \vec{H}(r)$ as well. So through cleverly introducing certain dielectric materials one can create specific distributions. "The Hermitian nature of the operator Θ leads to real eigenvalues. Further, since $\epsilon(r) > 0$ everywhere, Θ is positive semi-definite, and therefore all the eigenvalues are non negative. Further, any two eigenmodes with different eigenvalues are orthogonal." [26]. This shows further similarities to the *Hamiltonian Operator* in quantum mechanics. Analytic solutions to the equation 2.73 for arbitrary geometries are far from trivial. The main idea behind this project and illustrated in [27] is that the introduction of an hBN lens inside the cavity changes the 'photon potential' $\epsilon(r)$ and leads to specific electric field distributions. By 'hBN leans' is meant a microscopic lens form which consists purely of hexagonal Boron Nitrate. The specific forms analysed

²For the reader's wondering why the equation 2.73 is written with the magnetic field \vec{H} and not the electric field. This has something to do with the hermitian nature of the equation which is not given anymore if written for the electric field. Interested readers are referred to second chapter in [22] for a much more detailed treatment of the subject.

in this project will be discussed later in section 4.2.1.

Even though general analytical solutions to 2.73 are not possible a few special cases of relevance to the Fabry-Pérot cavities in this project will be discussed. In a planar geometry where the mirrors are separated by a distance d in a medium with refractive index n^3 . "The photon motion along the perpendicular z-direction is quantised as $q_z = \frac{\pi m}{d}$ " [4], where m is a positive integer. Each of these longitudinal modes q_z will have a frequency dispersion relation of the following form [4]:

$$\omega_{\text{cav}} = \frac{c}{n} \sqrt{(q_z)^2 + k^2} \approx \omega_{\text{cav}}^0 + \frac{\hbar k^2}{2m_{\text{cav}}} \quad (2.75)$$

This parabolic dispersion relation gives the photon an effective mass m_{cav} . This quantity is related to the cutoff frequency of the cavity $\omega_{\text{cav}}^0 = cq_z/n$ by the following expression

$$m_{\text{cav}} = \frac{\hbar n q_z}{c} = \frac{\hbar \omega_{\text{cav}}^0}{c^2/n^2}$$

Through longitudinal confinement the photons are given mass and concentrated between the mirrors.

To elaborate on this a little bit further "the electric field distribution $E(\vec{r}) = E_0\psi(\vec{r})$ is determined by a spatially varying mode function $\psi(\vec{r})$ " [20]. A Gaussian standing wave inside a general Fabry-Pérot with mirrors located at $x = (0, d)$ has a mode function given by:

$$\psi(\vec{r}) = \sin\left(\frac{2\pi x}{\lambda}\right) \exp\left(\frac{y^2 + z^2}{\omega_0}\right)$$

Where ω_0 is the *cavity waist* [23]. Without going into too much detail, in a planar Fabry-Pérot cavity with two parallel plane mirrors the curvature of both mirrors can be treated as infinite. As a result the ω_0 is also infinite, which simplifies the above expression to:

$$\psi(\vec{r}) = \sin\left(\frac{2\pi x}{\lambda}\right) \quad (2.76)$$

This longitudinal confinement is done by plane parallel Fabry-Pérot cavities and the main turning parameter here in the setup is the separation of the mirrors and their reflectivities. If the electric field distribution is to be manipulated further additional geometric features inside the transverse plane need to be introduced which confine the photons in both directions of the transverse plane. This change in geometry changes the spatial distribution the electric permittivity $\epsilon(r)$ in the master's equation 2.73 and reduces the dimension of the

³The setups studied in this project contain air between the two mirrors, so $n = 1$. However the n will be kept as a variable to keep the expressions somewhat more general.

cavity to zero.

An example of introducing transverse confinement in Fabry-Pérot cavities are *plane-concave Fabry-Pérot cavities*. These cavities are similar to the ones discussed previously, however a key difference is that one or both of the mirrors are curved. The basic geometry of a plane-concave Fabry-Pérot cavity is illustrated in Figure 2.9.

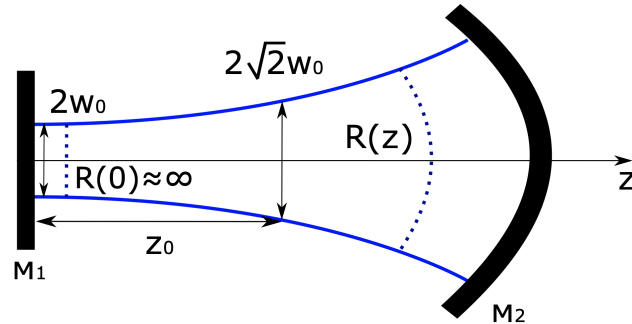


Figure 2.9. Illustration of a planar-concave Fabry-Pérot cavity where the second mirror M_2 is curved. The beam waist of a Gaussian mode is then drawn in blue to highlight the confinement of the photons underneath the dimple [2]

Even though plane concave Fabry-Pérot cavities are great in creating zero-dimensional micro-cavities. The main additional tuning parameters for this type of setup are the curvature radii R_1 and R_2 for the two mirrors. As these are only two parameters the setup is limited in its flexibility to create transverse cavity modes. A new approach to creating zero dimensional Fabry-Pérot cavities was made this year through the development of a new procedure to create fine structures and geometries with the material hexagonal Boron Nitrate [27]. The work laid the foundation of what could potentially become the next generation of optical micro-cavities. Through placing an hBN lens inside the cavity on top of one of the DBR mirrors the researchers managed to confine the light on top of the lens. This is illustrated in Figure 2.10. Because the method of shaping the hBN freeforms is very flexible this work lays the foundation of a whole new class of experiment with placing different types of hBN lenses and shapes inside Fabry-Pérot micro-cavities.

The main goal of this project was to build numerical models for Fabry-Pérot cavities within COMSOL and then simulate possible lens types. This work will be a key step in choosing which hBN geometries to investigate further inside these cavities.

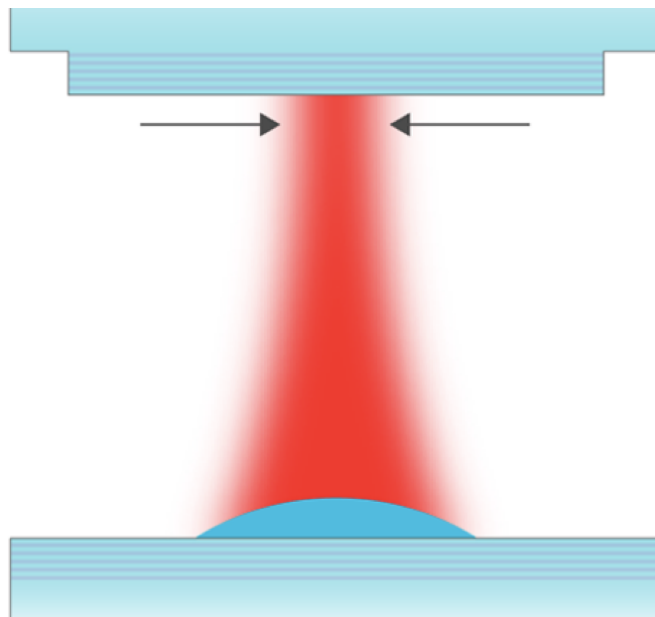


Figure 2.10. An illustration of an hBN lens inside the Fabry-Pérot micro-cavity. Marked in red is the concentrated electric field which can be seen to concentrate on top of the lens [27]

3 COMSOL Multiphysics[®]

COMSOL Multiphysics[®] is a software product which allows the user to numerically simulate physical systems. It has many applications in Physics and Engineering through solving the relevant differential equations on given domain with the *Finite Element Method (FEM)*. This software was chosen as it is able to solve Maxwell's equations numerically for arbitrary geometries and materials. This aspect was particularly relevant for this project since the idea was to build models, which could simulate arbitrary hBN structures inside a Fabry-Pérot cavity. The version utilised in this analysis was COMSOL 5.5. This chapter will be concerned with introducing the basic notions of the FEM. Moreover, the procedure of building a two dimensional Fabry-Pérot cavity will be discussed. Even though real Fabry-Pérot cavities are three dimensional objects the 3D simulations in COMSOL are much more computationally intensive. Since all three dimensional cavity geometries studied in this thesis were rotation symmetric around the propagation direction of the beam the decision was made to implement the simulations in a two dimensional geometry in COMSOL.

3.1 Theory on Finite Element Method (FEM)

Solving partial differential equations such as the Maxwell equations 2.1, 2.2, 2.3, 2.4 analytically can be cumbersome and for certain geometries downright impossible. When trying to solve a variational boundary value problem for a continuous solution numerically the computer discretises the system. This is important as computers are finite state machines and hence cannot compute continuous solutions. The objective of the FEM is then to provide an "algorithm for the computation of an approximate numerical solution as a function belonging to a subspace of the variational function space" [18]. The approximation is then done through minimising an associated error function to the problem with the calculus of variations.

The process of discretising the domain is called *meshing* and marks a key step in the Finite Element Analysis. Another key advantage of FEM as opposed to other numerical methods for solving PDE's such as finite differences is that "while the solution is computed, the mesh can be adapted in order to speed up convergence" [15]. The main idea behind meshing is

illustrated in Figure 3.1.

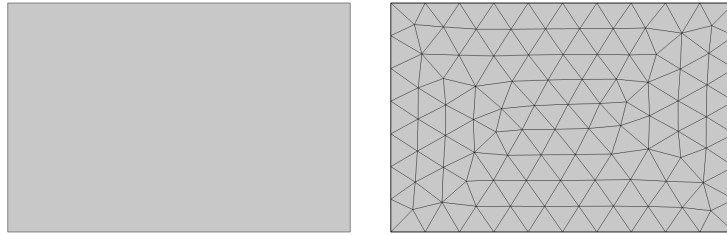


Figure 3.1. A simple example of meshing a rectangle geometry within COMSOL

As can be seen in Figure 3.1 the software slices the domain into triangles of a specified size automatically. The selection of shape and size done by the model builder as well as the procedure for meshing will be explained in more detail in the next section.

3.2 Building a 2D DBR cavity in COMSOL

As the majority of this project consisted of working with the simulation software, a brief outlook is given on the procedure of building Fabry-Pérot cavity setups within COMSOL Multiphysics®. Depending on the physical situation different modules within the COMSOL environment can be chosen. The modules concerned with electromagnetism are the following:

- AC/DC
- Radio Frequency (RF)
- Plasma
- Semiconductor
- Wave Optics
- Ray Optics

Out of these only the last two are designed for modelling optical systems. The Ray Optics module models the electromagnetic wave propagation using the ray tracing approach. "The propagating waves are treated as rays that can be reflected, refracted, or absorbed. This treatment of electromagnetic radiation uses approximations that are appropriate when the geometry is large compared to the wavelength." [8]. As the nanophotonic systems to be described in this project will be on length-scales comparable to the wavelength the conditions for this approximation will not be satisfied. Moreover, one aspect of the project consisted of varying the rayleigh length of the incoming Gaussian beam which also invali-

dates the ray approximation of the beam. Thus the Wave Optics module was used in this project. This module was specifically designed to "study electromagnetic wave propagation and resonance effects in optical applications" [9], which makes it ideal for an analysis of Fabry-Pérot cavities. The main two interfaces in the Wave Optics module were of concern for this project were:

- The Electromagnetic Waves, Beam Envelopes Interface
- The Electromagnetic Waves, Frequency Domain Interface

In the former is factors the electric field "into a product of a slowly varying envelope function (slowly on the scale of a wavelength) and a rapidly varying phase function" [12]. This was a again a condition which would not be satisfied in the Fabry-Pérot cavities to be modelled in this project. As a result the Wave Optics Frequency Domain interface was selected for this analysis. This is the most robust way of studying optical phenomena in COMSOL, when the systems are on the same length-scale as the wavelength. However, as fewer approximations were made by COMSOL in this interface the simulations were more computationally intensive. This section will be concerned with the general model used in this project. Later models which used one or multiple hBN lenses were deviations from this model.

To start modelling in COMSOL select *Model Wizard* and then the *2D* option for the spatial dimension. Next the Wave optics module is chosen and the initial study is set to the *frequency domain* interface. Other studies can be added as well, but this was not done during this project. In the *Global Definitions* section the following list of parameters are defined for the model:

Name	Expression	Value	Description
lda0	1[um]	1E-6 m	reference wavelength
n_l	1.4570	1.457	refractive index of SiO2
n_h	2.1205	2.1205	refractive index of Ta2O5
d_l_DBR	lda0 / (4 * n_l)	1.7159E-7 m	thickness SiO2 layer in DBR
d_h_DBR	lda0 / (4 * n_h)	1.179E-7 m	thickness TiO2 layer in DBR
f0	c_const / lda0	2.9979E14 1/s	referenc frequency
d_cav	16 [um]	1.6E-5 m	length of geometry
h_cav	30 [um]	3E-5 m	cavity width
lda0_min	1000.27[nm]	1.0003E-6 m	max Wavelength
lda0_max	1000.3[nm]	1.0003E-6 m	min Wavelength
N	15	15	number of Bragg pairs in DBR
d_layer	d_l_DBR + d_h_DBR	2.8948E-7 m	
d_PML_layer	d_layer * 2	5.7896E-7 m	depth of perfectly matched layer
f_max	c_const / lda0_min	2.9971E14 1/s	
f_min	c_const / lda0_max	2.997E14 1/s	
d_mirrors	3 [um]	3E-6 m	seperation of DBR - cavity height
d_lens	50[nm]	5E-8 m	thickness of hBn lens
circ_radius	50 [um]	5E-5 m	radius of circle used to create lens
n_hBn	2.0865	2.0865	refractive index of hBn at 1000nm

Figure 3.2. A list of all the model parameters

A few important parameters to note in Figure 3.2 are:

- $lda0$: Reference Wavelength to which the micro-cavity will be tuned
- n_l : Lower refractive index of the two materials that will make up the DBRs. Here the material was chosen as Silicon dioxide
- n_h : Higher refractive index of the two materials that will make up the DBRs. Here the material was chosen as Tantalum pentoxide
- N : Number of Bragg pairs in the DBR. A Bragg pairs is the union of layer a low refractive index and high refractive index.
- $d_{mirrors}$: Spacing between the two DBR's and hence defines the cavity length.
- $lda0_{min}$: Lowest wavelength of incident radiation we wish to study
- $lda0_{max}$: Highest wavelength of incident radiation we wish to study

The parameters $lda0$, n_l , n_h , N and $d_{mirrors}$ were not changed in any of the models. The frequency domain interface in the COMSOL wave optics module performs a parametric sweeps of different frequencies for the incident beam. This means in a given frequency interval a selected number of equally spaced frequencies is chosen to be simulated. The variables $lda0_{min}$ and $lda0_{max}$ were used to specify this frequency interval.

The rest of the parameters are either directly derived from the above or are arbitrary chosen to make the geometry work within COMSOL. The Figure 3.3 depicts the geometry. In Figure 3.3 the lens is already introduced. As the lens is not relevant for the next sections its introduction into the geometry will be explained later in section 4.2.1.

In COMSOL areas within the model are referred to as *domains* while lines are called *boundaries*. It can be seen in Figure 3.3 that the entire geometry is fitted within a large rectangle of width d_{cav} and height h_{cav} . This rectangle serves as a background for the entire model. The two lines on either side of the rectangle are used for meshing and boundary conditions. These lines are of width $d_{PML_layer}/2$ and can be set inside rectangle under the feature *layers* in COMSOL. The distributed Bragg reflectors are built by first introducing two rectangles with the height of the large rectangle and widths d_l_DBR and d_h_DBR respectively. The width of these layers corresponds to the quarter wavelength spacing as described by equation 2.64. The first DBR is then build by unifying the first two layers and then using the *array* tool of COMSOL geometry. This feature duplicates the input object, in our case this would correspond to creating 15 pairs of the two layers. In a next step the first DBR is mirrored using the *mirror* tool to copy the first DBR and create a cavity.

Once the geometry is set up in COMSOL the next step is to assign the materials for each domain. In the figure 3.3 is possible to see that the original large rectangle is divided into

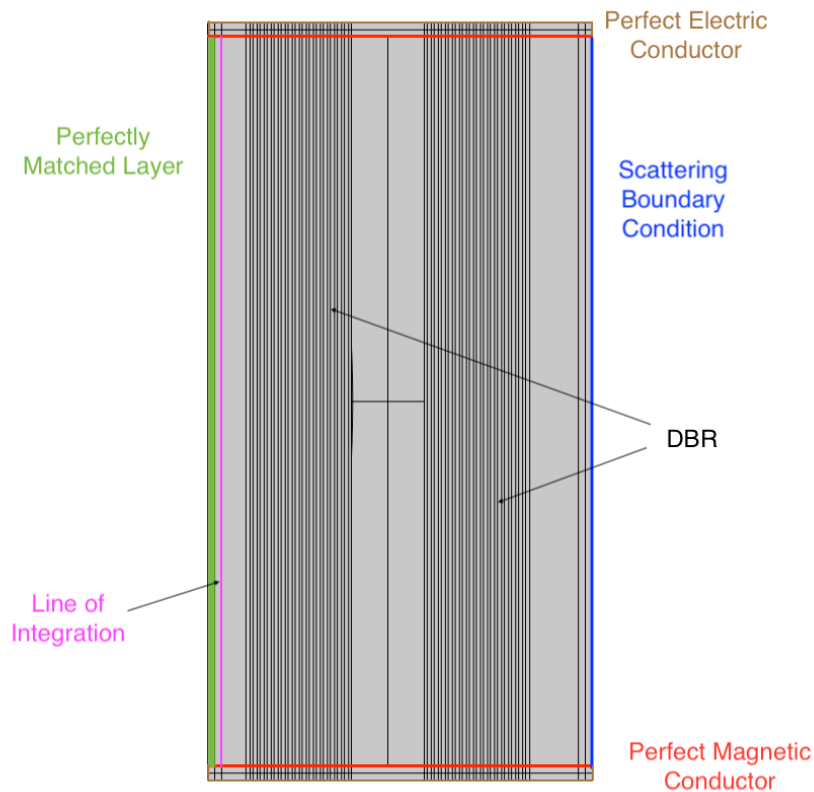


Figure 3.3. The geometry of a 2D DBR Fabry-Pérot cavity in COMSOL as well its boundary conditions are depicted

many domains, 340 to be precise. Now each of these 340 domains needs to be assigned a material. For this the refractive indices n_l and n_h were defined in the model parameters section in Figure 3.2, these correspond to the refractive indices of SiO_2 and Ta_2O_5 . They were defined as variables so that they can easily be changed in case different materials are used for the DBRs. To add these materials in COMSOL go to the *Materials* toolbar and click add material. Then type in the relevant refractive index using the variables from the global parameter list in Figure 3.2. The material air, which will make up most of the domains in the model, is already included in the COMSOL software. Air is also chosen as the material between the DBR mirror, as this was also done in the experiment on zero-dimensional Fabry-Pérot cavities using hBN lenses [27]. The hBN inside the lens will be added later, so for now the lens will also be designated as air in order to test the models using existing numerical tools as shown in section 4.1.

The next step is to start thinking about how to excite the relevant physics into the model. In this first model a plane wave as described by equation 2.26 is send into the model. In reality one would typically place a laser, or some other photon source, in front of the cavity. To realise this within COMSOL without including an entire model of a laser in the

simulation the *Scattering Boundary Condition* is used. The rightmost boundary is chosen for the scattering boundary condition as depicted in Figure 3.3. In order to send in a plane wave select the *incident field* as *Wave given by E-field*. The following specifications for the plane wave were set to:

$$\mathbf{E}_0 = \begin{pmatrix} 0 \\ 0 \\ 1 \end{pmatrix} \quad \text{and} \quad \vec{k}_{\text{direction}} = \begin{pmatrix} -1 \\ 0 \end{pmatrix}$$

Through these specifications the incident beam will propagate through our setup from the right side to the left. In reality the cavity setup will be placed inside a laboratory surrounded by air. Neglecting outside environmental effects the photons which bounce off the system will leave the cavity and escape from the system. However inside the simulation it is not possible to create an infinitely extending micro-cavity so artificial truncation of the domain through boundary conditions needs to be introduced on each side of the rectangle in Figure 3.3. In order to prevent the electric field to accumulate at the left side of our cavity. An artificial domain in the leftmost domain. This so called Perfectly matched layer (PML) "absorbs all radiated waves with small reflections" [12] and acts like a 'sink' for the electric field in the simulation. The PMLs do so by applying a "coordinate scaling to a layer of virtual domains surrounding the physical region of interest." [12].

An important part of the analysis in 2.3 was the transmission coefficient of a micro-cavity. This was due to the fact that a peak in the transmission spectrum corresponds to a resonant mode in the cavity. In order to get a quantitative measurement for the transmission in the model a line integration needs to be performed in the left region of the cavity. The line right in front of the PML layer was chosen for the electric field norm squared $|\vec{E}|^2$ to be integrated over. This line is highlighted in pink in Figure 3.3. From equation 2.30 it is clear that the resulting integral would be proportional to the integral of the intensity. The same integration is performed for the incoming beam and the transmission coefficient is then given by their ratio.

It was attempted to surround the entire domain with PMLs however this did not yield the desired effect as the resulting electric field distribution across the domain was not symmetric anymore.

The two other boundary conditions considered in this project were:

- Perfect Electric Conductor (PEC)

- Perfect Magnetic Conductor (PMC)

Out of these two only the Perfect Magnetic Conductor is of relevance to this model. The Perfect Electric Conductor boundary conditions is technically still part of the model, but have no effect on the system. Even though the PEC is not relevant for this model its main functionalities will still be explained in case future models wish to include this boundary condition.

The *perfect electric conductor (PEC)* boundary conditions enforces the following on the boundary.

$$\vec{n} \times \vec{E} = 0$$

The tangential component of the electric field is then set to zero. The PEC is particularly good at modelling lossless metallic surfaces. Moreover it imposes a symmetry for the magnetic fields and an anti-symmetry for the electric fields [12]. An illustration of the the PEC is given below in Figure 3.4.

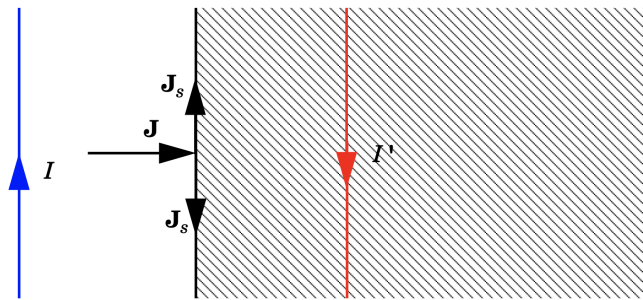


Figure 3.4. "The perfect electric conductor boundary condition is used on exterior and interior boundaries representing the surface of a lossless metallic conductor or (on exterior boundaries) representing a symmetry cut. The shaded (metallic) region is not part of the model but still carries effective mirror images of the sources. Note also that any current flowing into the boundary is perfectly balanced by induced surface currents. The tangential electric field vanishes at the boundary." [12]

However the anti-symmetry of the electric field in the cavity is not what should happen in a symmetric Fabry-Pérot cavity. As a result the top and bottom edges of the cavity internal boundaries are set to the *Perfect Magnetic Conductor (PMC)* boundary condition, which is depicted in Figure 3.3. The PMC "implies that the solution is mirror symmetric about those planes" [7]. It does so by imposing the following on the boundary:

$$\vec{n} \times \vec{H} = 0$$

"On external boundaries, this can be interpreted as a "high surface impedance" boundary condition or used as a symmetry type boundary condition. It imposes symmetry for electric fields and electric currents. Electric currents (volume, surface, or edge currents) are not

allowed to flow into a perfect magnetic conductor boundary as that would violate current conservation" [12]. The PMC is also illustrated further in Figure 3.5.

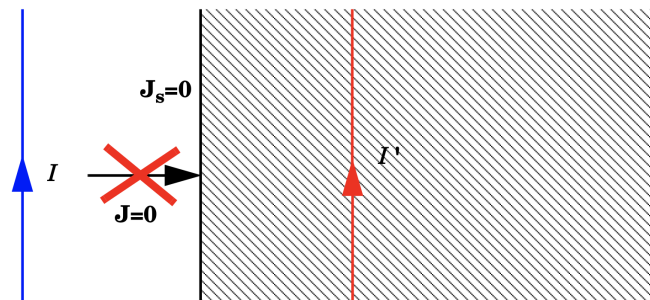


Figure 3.5. "The perfect magnetic conductor boundary condition is used on exterior boundaries representing the surface of a high impedance region or a symmetry cut. The shaded (high impedance) region is not part of the model but nevertheless carries effective mirror images of the sources. Note also that any electric current flowing into the boundary is forbidden as it cannot be balanced by induced electric surface currents. The tangential magnetic field vanishes at the boundary. On interior boundaries, the perfect magnetic conductor boundary condition literally sets the tangential magnetic field to zero which in addition to setting the surface current density to zero also makes the tangential electric field (and in dynamics the tangential electric field) discontinuous" [12]

In Figure 3.3 the PMC boundary condition is not set on the exterior boundaries of the rectangle. Instead the PMC boundaries enclose the cavity from the top and bottom. The exterior boundaries are still set as PEC due to the fact that COMSOL requires all exterior boundaries to be set a boundary condition. For these top and bottom exterior boundaries the PMC could have been chosen as well. The fact that this models still includes the PEC is a relic from older models, which used PMLs and was kept to give the model builder some more freedom with the geometry. The electric field distributions in all models showed that the electric field norm in domains behind the PMC boundaries equals zero. The PEC boundaries can thus be ignored and the cavity can be treated as if it ends with the PMC boundaries.

COMSOL uses the Finite Element Method (FEM) to calculate a numerical solution of the Maxwell equations for the model. In order to apply the FEM the domain needs to be discretised into smaller pieces as illustrated in 3.1. This is a crucial step which can lead to many problems if done incorrectly. One needs to consider the following:

- How the geometry is divided
- With what shape or element type the geometry is divided
- The size, density, and number of elements in the geometry
- The element quality

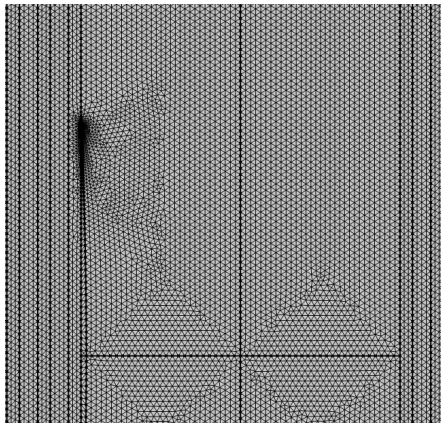
There is the option to do a physics controlled mesh and let COMSOL do the meshing. Unfortunately this rarely works perfectly and further analysis is needed. It is recommended though to start the user-controlled meshing from this physics controlled one.

The mesh generator discretises the domains into triangular or quadrilateral mesh elements. If the boundary is curved, these elements represent only an approximation of the original geometry. The sides of the triangles and quadrilaterals are called mesh edges, and their corners are mesh vertices. A mesh edge must not contain mesh vertices in its interior.

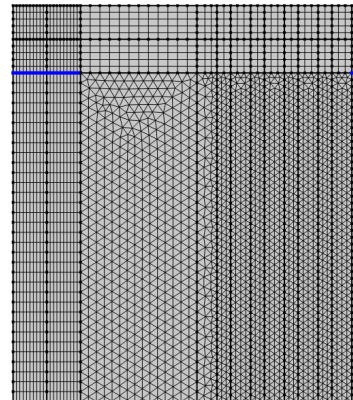
For this model the following mesh features within COMSOL were used [6]:

- *Mapped* : A meshing technique generating a structured mesh with quadrilateral elements for 2D or 3D models.
- *Free Triangular*: A free meshing technique generating an unstructured mesh with triangular elements for 2D or 3D models.
- *Distribution*: This feature is for boundaries and used to link the meshing of the domains on either side of the boundary.

There are many more mesh feature, however most of them are for three dimensional models. Any model implemented in two dimensions can be done very well using just these three mesh features above. The resulting mesh for our model looks like follows:



(a) Center of model



(b) Top left corner of model

Figure 3.6. Examples of the meshing inside the geometry

Plotting the mesh of the entire geometry was unfortunately not very insightful due to the small meshing size. Therefore Figure 3.6 depicts two selected regions.

Figure 3.6a depicts the fine triangular mesh in the center of the cavity. It can also be seen that at the end of the lens the meshing gets very fine. The COMSOL software does this to ensure that even the smaller domains are meshed properly. So that no boundary can be contained within a mesh triangle. In Figure 3.6b the mapped mesh to be seen in

the boundaries of the cavity. It can also be noted that COMSOL automatically creates a smooth transition from the finer mesh in the cavity to a more courser mesh outside of the cavity. Furthermore a distribution is highlighted in blue in order the match the meshing of the PML layer to the other mapped mesh domains.

Meshing a given geometry can bring some challenges. Firstly is noted that in the perfectly matched layer domain the mapped feature of meshing needs to be used. This is recommended by COMSOL as the elements should not get stretched or distorted. As a result the Mapped feature for meshing are introduced in all PML domains. This will slice these domains in rectangles. As the transmission coefficient is very important for the analysis in this project and from equation 2.30 it is clear that the electric field amplitude squares is proportional to the intensity. An integration of that quantity will be performed on the left side of the cavity so this domain should be particularly well meshed. Furthermore, the distribution feature is introduced, which links the domain on both sides of the boundary and fixes the number of intersections on this boundary. In this example the distribution on the following boundaries introduces ten nodes, which refines the mesh on the domains adjacent to the boundary. These domains are now meshed very finely as well which is good for the integration. The rest of the system is modelled with the free triangular feature, which slices the domains in triangles. The resulting electric field distribution will be analysed in the next section and can be seen in Figure 4.2.

4 Results

The goal of this project was to analyse and simulate the effects of introducing hBN lenses of different shapes inside a planar Fabry-Pérot cavity to gain a better understanding of these types of zero-dimensional cavities. It is anticipated that this work will be used to simulate new shapes and forms of hBN structures before interesting ones are selected for fabrication and experiments in real cavities. These models are designed to assist future researchers in their study in this type of system.

The main outline for this chapter is the verification that the models build in 3 indeed describes a planar Fabry-Pérot cavity. Once this verification is complete the project proceeded in introducing an hBN lens into the system with Gaussian beams. In this analysis different curvatures of the lens were analysed to get a better understanding of the transverse confinement of the electric field. In a final step multiple lenses were introduced in order provide a starting ground for more abstract shapes. These main steps are written again in more compact form:

- Verification of model without lens using an existing modelling technique
- One hBN lens is introduced to the system
- Three different curvatures of one lens are analysed
- Investigation into the Rayleigh length of Gaussian beams
- Two and four lenses are placed inside the cavity

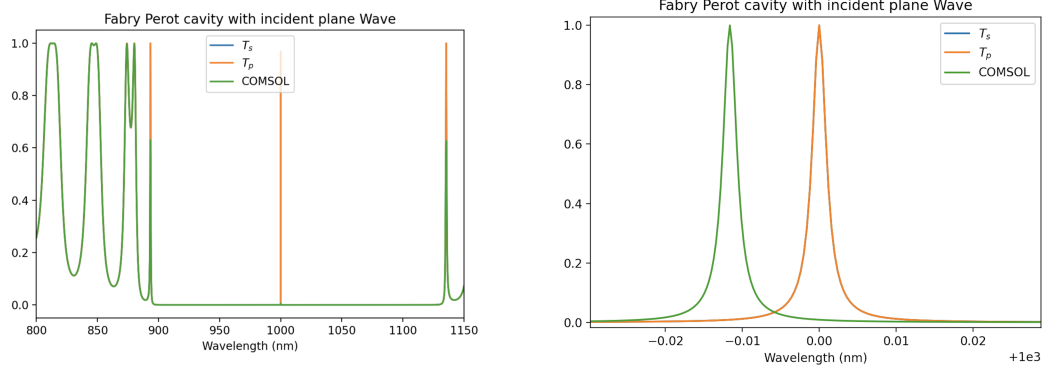
4.1 2D DBR cavity model without hBN lens

The transmission spectrum is a key characteristic of a planar Fabry-Pérot cavity as discussed in subsection 2.3. In order to verify that the model constructed in chapter 3 indeed models a planar Fabry-Pérot cavity its transmission spectrum was compared to an established numerical simulation tool for planar Fabry Perot cavities. The *TMM* python software package that implements the analysis for multi-layer stacks presented in 2.4 was programmed by the same person who provided the underlying analysis in [3]. As a planar

4 Results

Fabry-Pérot cavity is just a set of two DBRs it is perfectly possible to model this system using the TMM library.

The model from the previous chapter was computed in COMSOL and the transmission plot exported to a Jupyter notebook. A python program using the TMM software package computed the corresponding model and the two datasets was overlaid. The corresponding code used in this project can be found in Appendix A. For this demonstration the frequency range of $800nm - 1150nm$ was chosen. The overlay of the two datasets can be seen in Figure 4.1.



(a) Transmission plot for large wavelength range of $800nm - 1150nm$ (b) Transmission plot for large wavelength range near reference frequency of $1000nm$

Figure 4.1. Data overlay of the COMSOL and TMM python models

It is clear from Figure 4.1a that the COMSOL data in green matches the blue and orange data from the TMM model fairly nicely. T_s and T_p are the transmission coefficients for s- and p-polarised waves respectively, which were calculated in the TMM model. However for this setup both are identical, which is why the blue line cannot be seen. The reason why the green line does not match the orange line in all places is a result of the way the data is acquired. This COMSOL model uses the *frequency domain* interface, as explained in chapter 3. This interface performs a frequency sweep. For the given interval of frequencies it chooses a specified number equally spaced data points. In this simulation about 1500 were used. As this is a much less fine sweep than the TMM the overlay is not perfect and COMSOL misses the characteristic spike at the reference wavelength. The TMM library used about 150 000 data points for its parametric sweep in Figure 4.1a. Even though sweeps of this size are technically possible in COMSOL they are computationally extremely intense. This limitation of the frequency sweep presented a great challenge in the analysis of the models throughout the entire project. In order to more closely examine the characteristic spike of a DBR Fabry-Pérot cavity the region around the reference frequency was swept much more thoroughly. It can be seen that both models produce the same shaped spike. However there is a small deviation of about $0.012nm$. This deviation shows that the

COMSOL models are not perfect at replicating an ideal DBR cavity and this should be kept in mind when analysing the results. Even though there is some numerical error the deviation is relatively small, so the models are still able to provide rich insights into the physics of these systems. An assumption made in this project was that the deviation of $0.012nm$ is a systematic error of the COMSOL simulation system, so that the models could still be compared to one another. However some more investigation into this is needed.

The Transmission coefficient was obtained through integrating the norm of the electric field squared $|E|^2$ on both ends of the cavity. According to equation 2.30 $|E|^2$ is proportional to the intensity. As the region in front and behind the cavity both consist of air the ratio between the two integrals of $|E|^2$ is exactly the transmission coefficient. On a side note here the incoming electric field amplitude of the plane wave was chosen to be one, $|E_0| = 1$, so the calculation of the transmission coefficient can be simplified by simply dividing the integral of $|E|^2$ by the width of the cavity.

The peak occurred at $999.988nm$ or $299.796THz$. The FWHM was calculated as $6.327 * 10^8 Hz$. This results in a Q-factor of:

$$Q_{COMSOL} = \frac{2.9976 * 10^{14}}{6.327 * 10^8} = 473836 \approx 474\ 000$$

The Q-factor of the corresponding TMM model with $FWHM = 0.00218nm$ is given by:

$$Q_{TMM} = \frac{1000nm}{0.00218nm} = 458716 \approx 459\ 000$$

It can be seen that Q_{COMSOL} and Q_{TMM} are not exactly equal. This is likely due to errors in the frequency sweep as some data interpolation had to be done to obtain the numbers above. However the Q-factors are in the same ballpark which again reassures that the COMSOL model is indeed modelling what it claims to.

As explained in section 2.3 the resonant frequencies of a planar Fabry-Pérot cavity are exactly the frequencies for which the transmission spectrum peaks. Plotting the corresponding electric field distribution of the frequency corresponding to the peak in the transmission plot in Figure 4.1 can be seen in Figure 4.2. It is noted that sometimes the Q-factor is calculated through the frequency and on other times through the wavelength, both are equivalent as the equations 2.61 and 2.63 show. This was a result of different conventions used in different models.

The peak electric field norm depicted in 4.2 is about $273V/m$, which is a significant increase from $|E_0| = 1V/m$ so the resonant mode is indeed amplifying $|E|$ inside the cavity.

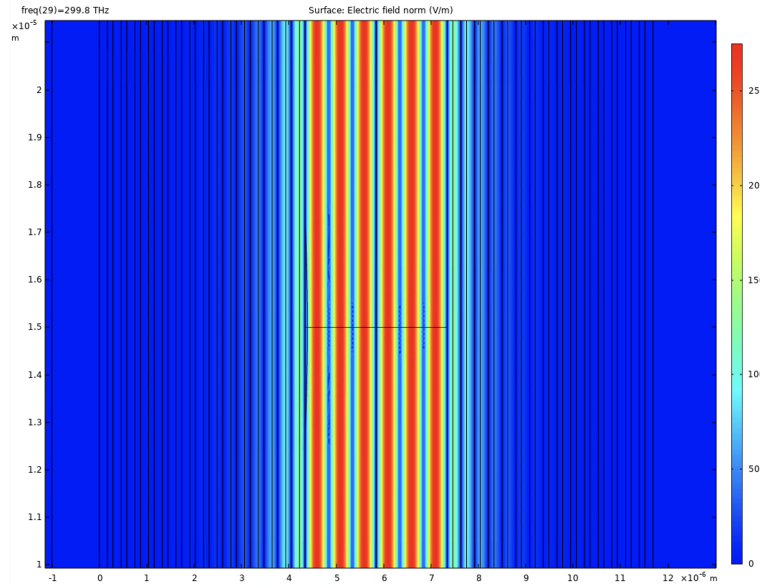


Figure 4.2. The electric field distribution is plotted at the resonance frequency of the cavity. This frequency is the peak in the transmission spectrum

In this geometry of a planar Fabry-Pérot cavity clearly six peaks in the electric field norm can be identified, which results from the longitudinal confinement of the photon field. This can be explained by considering equation 2.76 again:

$$|\psi(\vec{r})| = \left| \sin\left(\frac{2\pi x}{\lambda}\right) \right|$$

Here the separation of the mirrors is set as $d = 3000\text{nm} \approx 3\lambda$. So $x \in [0, 3\lambda]$ which using the above spatial dependence of the electric field yields to six peaks. Some care needs to be taken when considering this formula though as it's derivation considers mirrors located at exactly $x = (0, d)$. However with the DBRs considered in this project there is some leakage of the electric field into the DBRs, which can also be seen 4.2. In order to properly apply the formula 2.76 the effective length d_{eff} , ($d_{eff} > d$), of the DBRs needs to be considered. The setup is symmetric in the y -Direction which results in an electric field norm in Figure 4.2 that is symmetric in the y direction. The confinement of the photon field is thus only longitudinal.

4.2 Zero dimensional DBR cavities with one hBN lens

So far the models discussed were concerned with planar or two-dimensional Fabry-Pérot cavities. A next step in the project was to introduce a lens made of hexagonal Boron Nitrate (hBN), which is placed inside the cavity. The idea is that this lens will undo the setup's translational in-variance in the direction perpendicular to the x axis and thus create trans-

verse confinement of the electric field. The transverse confinement for the photon field effectively reduces the dimension of free movement for the photons to zero.

The lens is introduced in the COMSOL geometry through first creating a circle of radius $circ_radius + d_lens$ using the parameters from Figure 3.2. Then a rectangle of width d_lens and height of the cavity itself is build. The lens is then obtained through intersecting these two objects using the corresponding feature in COMSOL. The procedure is illustrated in Figure 4.3.

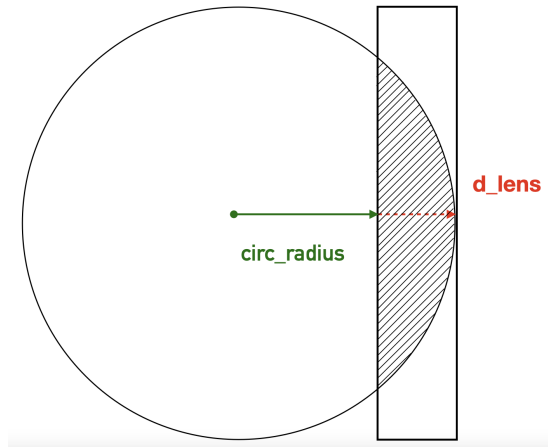


Figure 4.3. The lens is created by intersecting the circle and the rectangle

Both the circle and the rectangle need to be positioned appropriately in order for the lens to be situated right on top of the left DBR mirror. At this point it is noted that $circ_radius \gg d_lens$, so the curvature of the lens is mainly determined by the value of $circ_radius$. This will become significant when different lens curvature are analysed.

The refractive index for hBN was set to $n_{hBN} = 2.0865$ [32], which is the material's refractive index at the reference wavelength of $1000nm$. The refractive index is kept constant for all frequencies in the simulation. Since the system is examined in a wavelength range close to the reference wavelength this approximation is valid. However introducing a frequency dependent refractive index might be a good improvement for future models. The implementation of the lens into the model was fairly simple as the geometry for the lens was already introduced in the model discussed in chapter 3. The only thing needed to be done was to change the material from air to hBN in the relevant domains.

For the rest of the analysis the simulations will use Gaussian Beams as opposed to plane waves. Gaussian beams were discussed in subsection 2.2. These beams are a much better approximation for an incoming laser beam, so the comparison of results from the simulation with experimental data on hBN lenses in Fabry-Pérot cavities such as [27] are more valid. The reason why Gaussian beams were not considered before is that the TMM

library used to check the previous model uses plane waves. The Gaussian beams were introduced through the *Scattering Boundary Conditions* by selecting *Gaussian beam* in the *incident field* box. The initial electric field amplitude \vec{E}_0 and direction of the wavevector \vec{k}_{dir} were the same as for the plane wave model discussed in section 3.2. The distance to the focal plane $\rho_0 = 0$ so that the Gaussian beam would be centered at the boundary. The beam radius $\omega_0 = 20\pi/k$, which is the standard setting in COMSOL. In subsection 4.2.3 some investigation into the ω_0 parameter will be done.

4.2.1 Introduction of the hBN lens

The first hBN lens to be considered was defined through setting the two relevant parameters as $circ_radius = 50\mu m$ and $d_lens = 50nm$. These values were chosen arbitrarily and will serve as a reference to the other models. Since over the course of this analysis the parameter $circ_radius$ was varied so $circ_radius = 50$ will be written more frequently to remind the reader of the curvature.

As can be seen in Figure 4.4 the lens is situated on top of the left DBR mirror and about $4.47\mu m$ wide in the geometry.

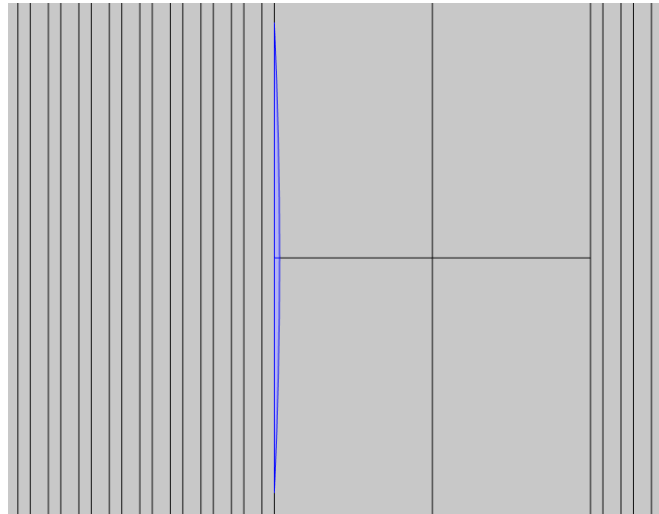


Figure 4.4. The first hBN lens in the Geometry

The project proceeded in analysing the transmission spectrum in order to find the resonance frequencies.

Similar to the Figure 4.1 the transmission peak is missed in the large wavelength sweep on the left in Figure 4.5a, so it is plotted again on the right. A few interesting things can be noted already from 4.5. Firstly, the transmission peak is still very close to one, however at close inspection smaller than in 4.1b. Moreover, the peak shifted in wavelength and is now slightly larger than the reference wavelength of $1000nm$. The peak has a value of

4 Results

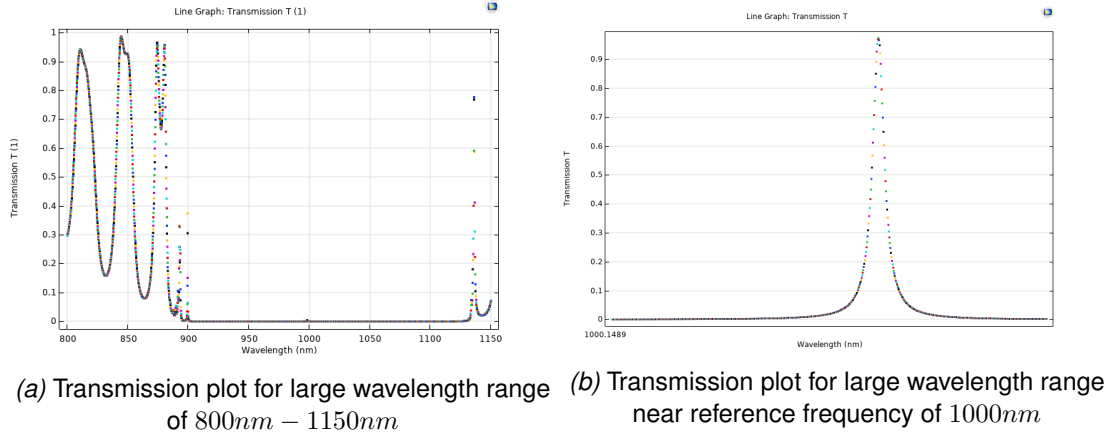


Figure 4.5. Transmission spectrum for one hBN lens with $circ_radius = 50\mu m$

$T = 0.97$ and occurs at $1000.193nm$ or $299.735THz$. The Full Width Half Maximum is given by $FWHM = 6.805 * 10^8 Hz$ and the Q-factor as follows:

$$Q = \frac{2.99735 * 10^{14} Hz}{6.805 * 10^8 Hz} = 440431 \approx 440\ 000$$

The Q-factor is still in similar range to the Q-factor seen in the plane wave and TMM model, though slightly smaller.

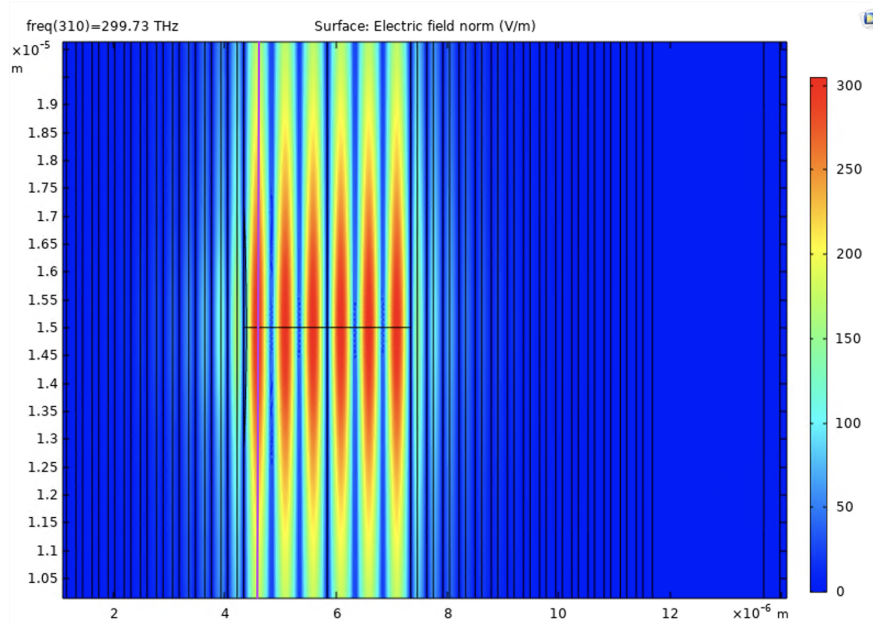


Figure 4.6. Distribution of the electric field norm at the resonance frequency of the zero dimensional Fabry-Pérot cavity with one hBN lens at $circ_radius = 50\mu m$

In Figure 4.6 the electric field distribution is displayed at the resonance frequency. Firstly the six peaks in the longitudinal direction of the beam can be observed again, which is

4 Results

similar to what could be observed in Figure 4.2. A qualitative explanation why a similar longitudinal structure might be expected is that the hBN lens is $50nm$ thick. This represents $1/60$ the length of the cavity. Moreover, the refractive index of the hBN used is $n_{hBN} = 2.08626$ the layer of Ta_2O_5 which sits right behind the lens has a refractive index $n_h = 2.1205$. Both refractive indices are not too different, so the changes to $\epsilon(r)$ might be so small that the change in the resulting electric field distribution from the master's equation 2.73 in the longitudinal direction might just be given by a small perturbation.

A key difference in the Figure 4.2 and 4.6 is the electric field distribution in the transverse direction. A line cut of the electric field distribution is taken at one of the peaks in the x-direction as highlighted by the purple line in Figure 4.6 results in the following plot:

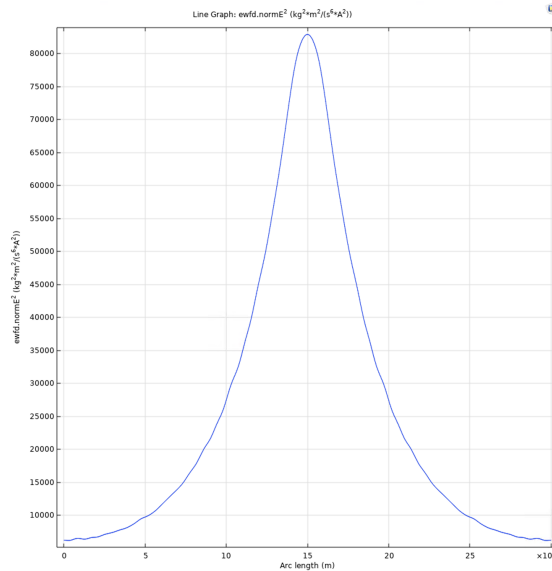


Figure 4.7. A vertical line cut of the electric field distribution squared across the entire cavity shows the fundamental (0,0) Gaussian mode

The parameter *Arc length* is standard in COMSOL and in this case refers to the vertical height. So an Arc length of zero corresponds to the position in the model, where the vertical line crosses the bottom of the cavity while the maximum Arc length corresponds to the top. This plot clearly shows a peak in of the electric field distribution right in front of the lens. The vertical profile depicted in Figure 4.7 stands in significant contrast to what could be observed in Figure 4.2. The introduction of the $circ_radius = 50\mu m$ hBN lens confines the electric field in the transverse plane. In fact Figure 4.7 looks a line cut of the fundamental Gaussian mode depicted in Figure 2.2. This is similar to the experimental data gathered by Lassaline and collaborators [27], who also measured the fundamental transverse mode. In this project it was attempted to find more Laguerre-Gaussian transverse modes but no other clear modes could be found. A possible explanation for this is that the corresponding transmission peaks were missed in the frequency sweep.

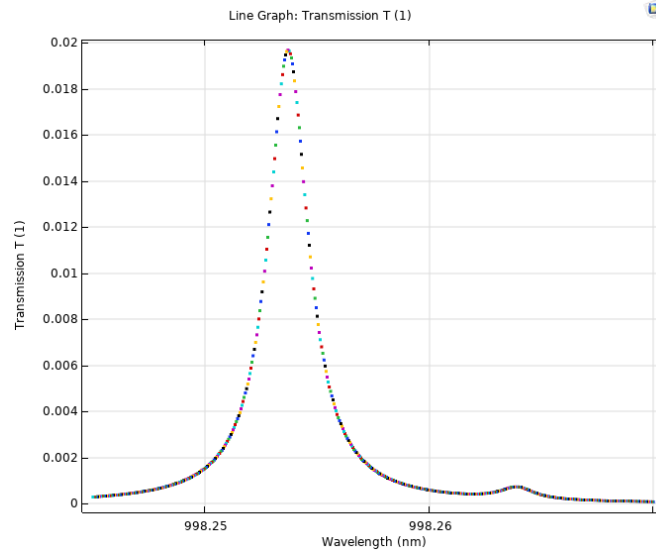


Figure 4.8. Zoomed in Transmission Plot to highlight the second peak.

A second transmission peak could be found located at 998.254nm or 300.317THz . As can be seen in Figure 4.8 this transmission peak is much smaller with peak transmission of $T = 0.0197$. Using the data above the full width half maximum was calculated, $FWHM = 6.543 * 10^8$. From this the Q-factor is given by:

$$Q = \frac{3.00317 * 10^{14}\text{Hz}}{6.543 * 10^8\text{Hz}} = 458971 \approx 459\,000$$

The Q-factor again of a similar scale to the ones already seen.

The Figure 4.9 shows the electric field distribution at the frequency of the transmission plot depicted in Figure 4.8.

A number of interesting features can be noted about this distribution. Firstly, this frequency seems to correspond to a different longitudinal mode, as the sinusoidal peak structure from Figure 4.6 is no longer present. Even though that is the case the electric field distribution still exhibits a symmetry across the vertical centered line. Another key difference is that there seems to be some periodicity in the occurrence of the peaks in the transverse plane. In order to analyse the transverse modes further vertical line cuts were taken through each of the first three longitudinal peaks as indicated by the red lines in Figure 4.9. The plots in Figure 4.10 show these line cuts.

All of these plots show the slightly periodic nature of this transverse mode. Another interesting feature is that the electric field is weakest right in front of the lens, which stands in direct contrast to what could be seen in the fundamental Gaussian mode in Figure 4.6. The

4 Results

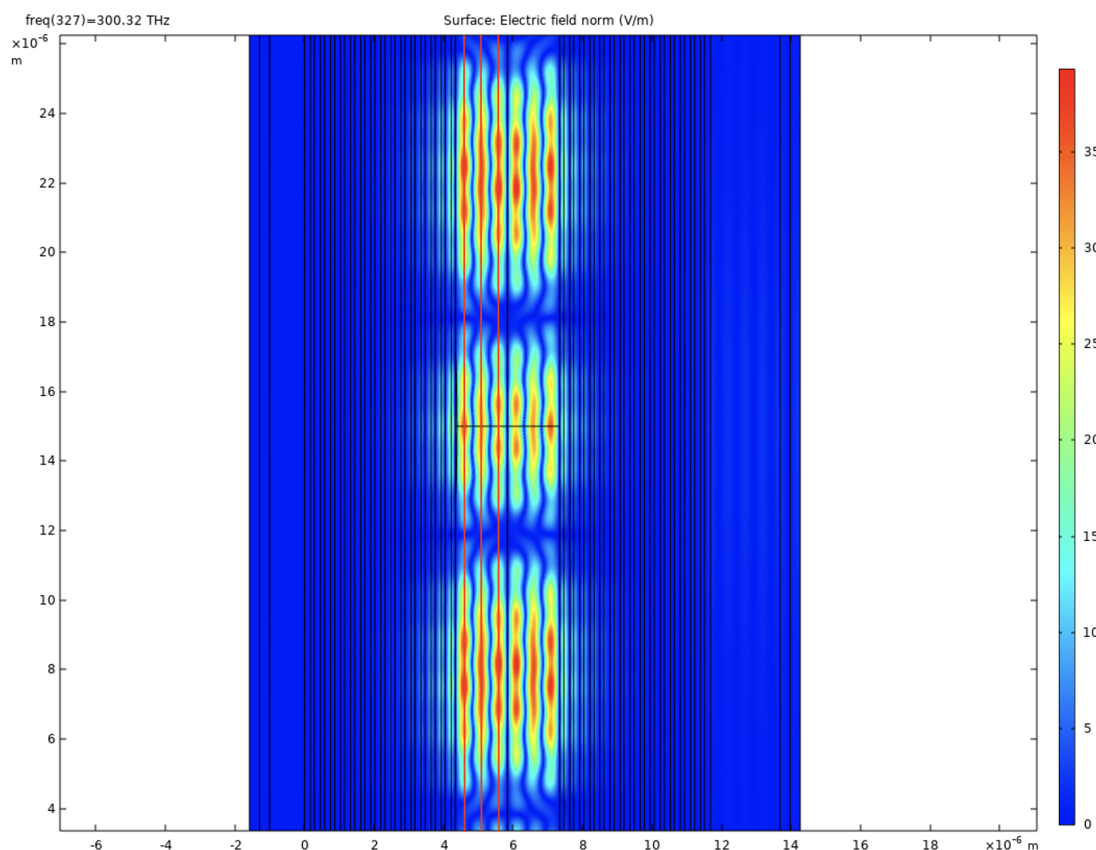


Figure 4.9. Electric field distribution of a second transmission peak located at 998.254nm

transverse field distribution in front of the lens corresponds to the middle peak in all three plots. Moreover, it is not yet clear which transverse Gaussian mode/modes the Figures 4.10a, 4.10b and 4.10c correspond to. The plots suggest that depending on the wavelength the light is focused on the lens or on specific other sections of the cavity. One could also make the argument that this mode is indeed non physical. An idea of how to gain some insight into this hypothesis would be to increase the vertical height of the cavity and see whether the period nature of the transverse mode change in any way. If the transverse electric field distribution still changes for relatively large vertical cavity heights the mode is likely non-physical. Due to time constraints this was not done during the project.

As this second cavity mode did not exhibit a transmission peak of height comparable to the first, the Free Spectral Range and Finesse could not be calculated for this cavity. It was attempted to find another transmission peak which would have a similar height to the fundamental mode. This was however not successful. A possible reason for this is that the parametric frequency sweep of the *frequency domain interface* missed these relatively small peaks. Some further investigation is needed to verify whether these peaks exist or not.

4 Results

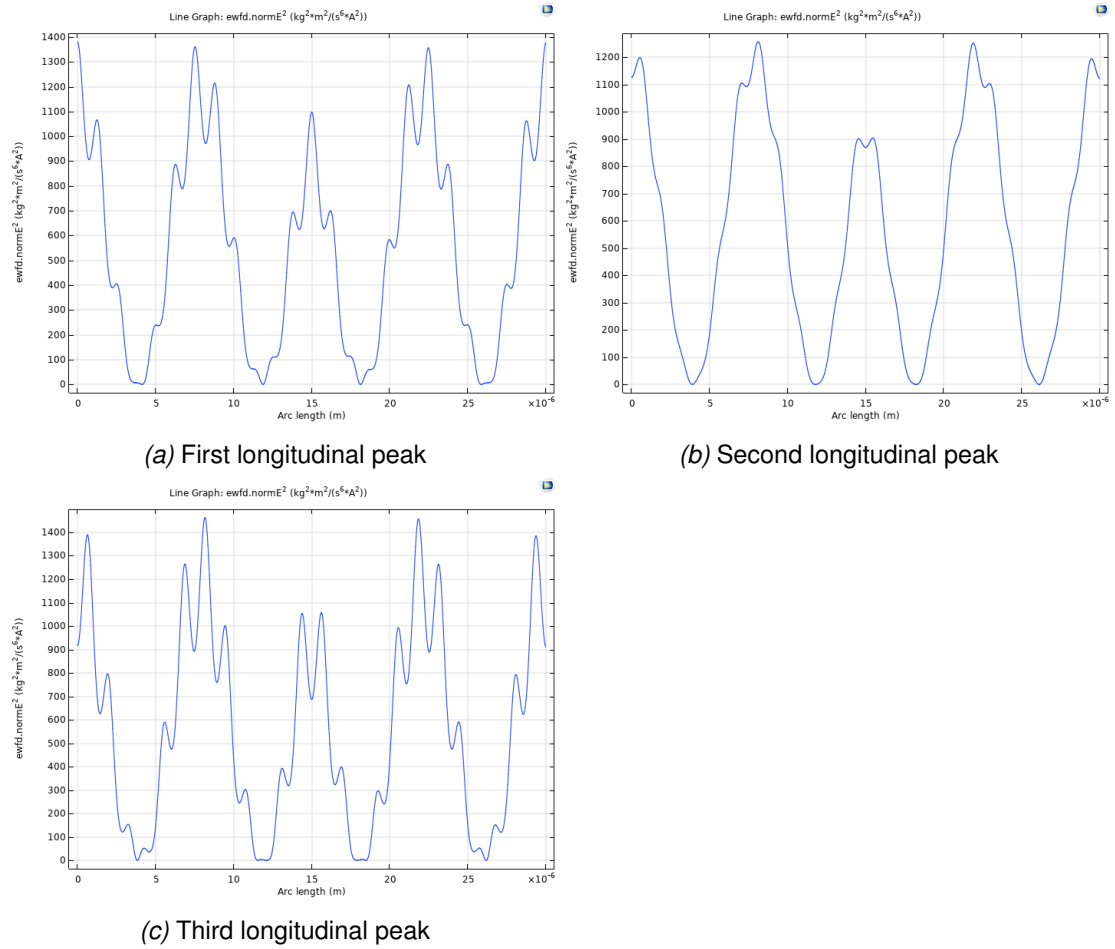


Figure 4.10. Vertical lines cuts of the electric field distribution squared at a second smaller resonance peak

4.2.2 Dependence of photon confinement on curvature of lens

In order to gain some more insight into the hBN lens zero-dimensional Fabry-Pérot, the dependence of the electric field distribution on the curvature of the lens was investigated. For this two new lenses were placed in two separate models. These new models were identical to the one discussed previously with the exception that the radius of the circle used to create the hBN lens geometry was altered. Previously the circle radius was given by $circ_radius + d_lens$. The latter parameter was kept constant at $d_lens = 50nm$ in order to have the same lens thickness in all three models.

In the previous model the circle radius parameter was set as $circ_radius = 50\mu m$. The two new models created for this investigation will be abbreviated as follows:

- MC Model: model for lens with more curvature, $circ_radius = 15\mu m$
- LC Model: model for lens with less curvature, $circ_radius = 100\mu m$

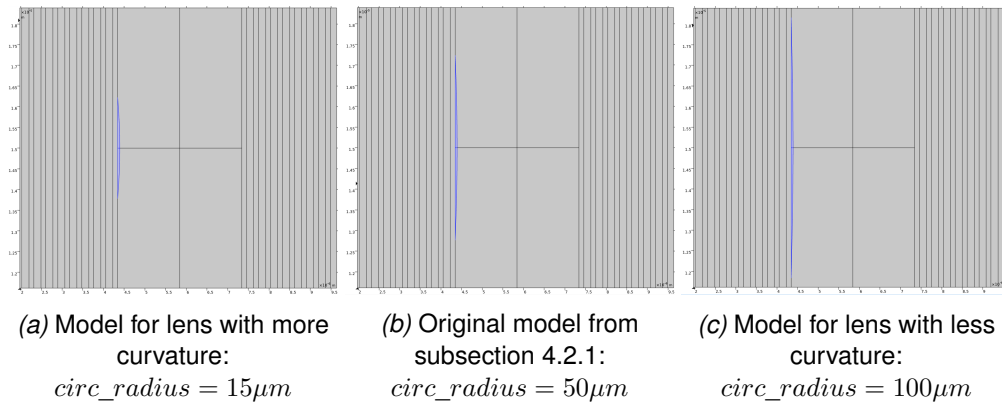


Figure 4.11. The three differently curved hBN lenses (blue) depicted inside their respective geometry

These specific values for $circ_radius$ were chosen rather arbitrarily and simply supposed to illustrate the principle of changing the curvature.

Repeating the analysis done in subsection 4.2.1, a small wavelength range around the reference wavelength of $1000nm$ is swept in each model to find the fundamental Gaussian mode in the transmission spectrum. The transmission peaks for the three models occurred in the at the following wavelengths:

- MC model: $1000.074nm$
- original model: $1000.193nm$
- LC model: $1000.320nm$

Even though the deviations in these resonance wavelengths are small a trend in the data can be observed. The more curved the lens is the smaller is its resonance wavelength. These three data point are not enough to derive a general formula. A qualitative explanation could be that a more curved lens confines the photon field in a smaller potential in the transverse plane, so one would expect smaller wavelengths for the stable modes.

The transmission peak in the MC model occurs at $1000.0743nm$ with a transmission coefficient of around 0.924. The Full Width Half Maximum can be calculated from this data to be $FWHM = 0.00219nm$. The Q-factor is then given by

$$Q_{MC} = \frac{1000.0743nm}{0.00219nm} = 455737 \approx 456\,000$$

This Q-factor is a little bit higher than the derived in the previous model where $Q \approx 440\,000$. However given that the deviation is not very large, this difference could have arisen due to calculation errors.

In the LC model the peak occurred at $1000.320nm$ or $299.697THz$ with a transmission coefficient of 0.963. The Full Width Half Maximum was $FWHM = 6.829 * 10^8 Hz$ and the Q-factor was then

$$Q_{LC} = \frac{299.697 * 10^{14} Hz}{6.829 * 10^8 Hz} = 438848 \approx 439\,000$$

The Q_{LC} is even closer to the original Q-factor. As all three Q-factors are fairly similar, the analysis done in this project would suggest that the Q-factor of the zero-dimensional hBN lens Fabry-Pérot cavity depends only weakly on the curvature of the lens.

In the next step the electric field distribution of both models is again plotted at the resonance frequency. The electric field distributions in both Figures 4.12a and 4.12b look fairly similar to the distribution in Figure 4.6. The transverse and longitudinal modes have some similarities. Especially the six peak structure discussed previously can be seen again. It can be noted however that the peak in the electric field norm is different in all three models. The highest peak is exhibited in the LC model and the lowest in the MC model. So the curvature also appears to have an impact on the magnitude of the electric field norm. This is especially significant if a cavity with immense electric field norms needs to be designed. Even though the three models covered so show that a smaller curvature increases the electric field norm, it is unlikely that this will continue indefinitely. An interesting investigation would be to test a wide range of curvatures to see whether an optimum can be identified. Due to time constraints this was not done during this project.

4 Results

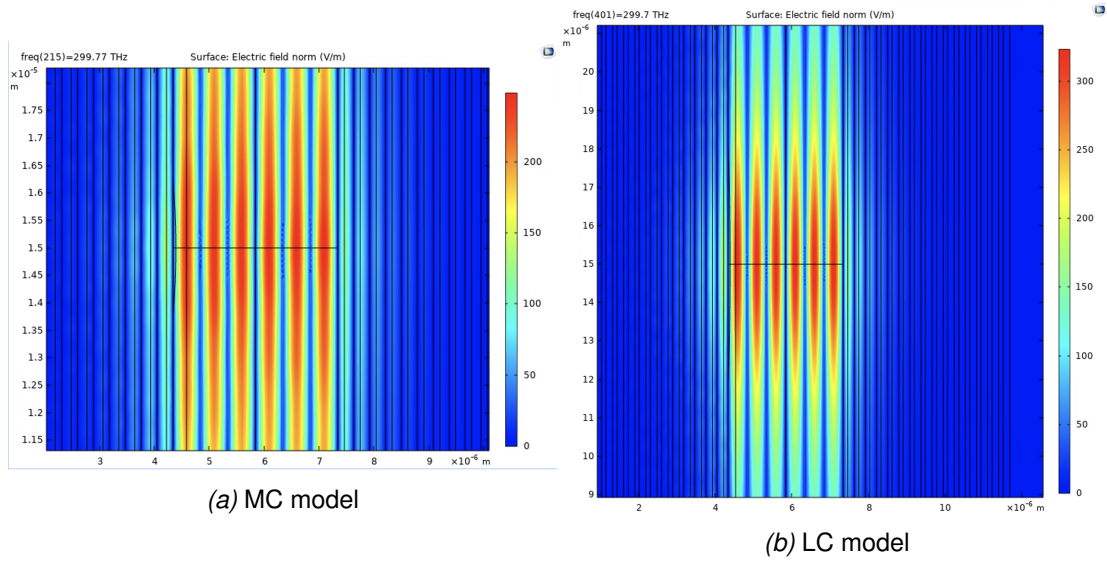


Figure 4.12. Electric field distributions of both models at the resonance frequency

To more closely examine the effect of changing the curvature of the lens again vertical line cuts are taken across the entire cavity in the electric field distributions in Figure 4.12.

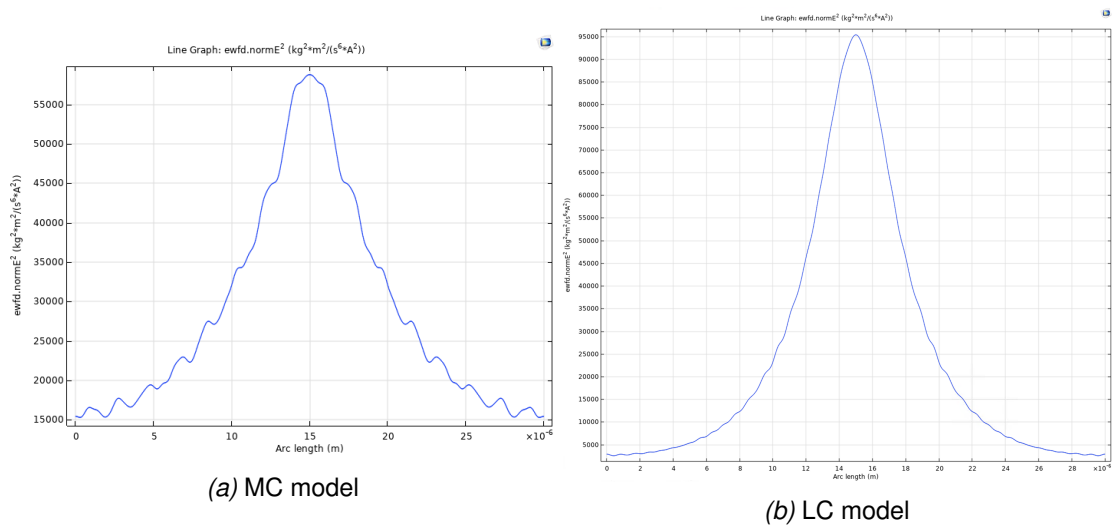


Figure 4.13. Vertical line cuts in the electric field distributions squared of both models at the resonance frequency

A vertical line cut across the entire cavity in the MC model where the x-coordinate was set so to the first of the six longitudinal peaks in the electric field distribution.

Drawing comparisons between the Figures 4.13 and 4.7 it is clear, that the transverse mode in the MC model looks a lot less smooth than the other two models. It could be that for the curvature in the MC model the fundamental Gaussian mode is located at a different

4 Results

resonance frequency. Another possible explanation is that this curvature is above some threshold after which no transverse fundamental Gaussian mode is possible, though this seems unlikely. It could also be a numerical error of the COMSOL simulation software. When the line cuts of the original and LC models, Figures 4.7 and 4.13b respectively, are examined more closely it is possible to see some of the 'shaky' characteristics which are observed to a much more extreme extent in Figure 4.13a. The three plots would then suggest that the more curved the lens is the more shaky its transverse modes become. Some more investigation into this dependence would be insightful.

In both the LC and MC models other smaller transmission peaks could be identified. Both exhibited fairly counter intuitive electric field distributions.

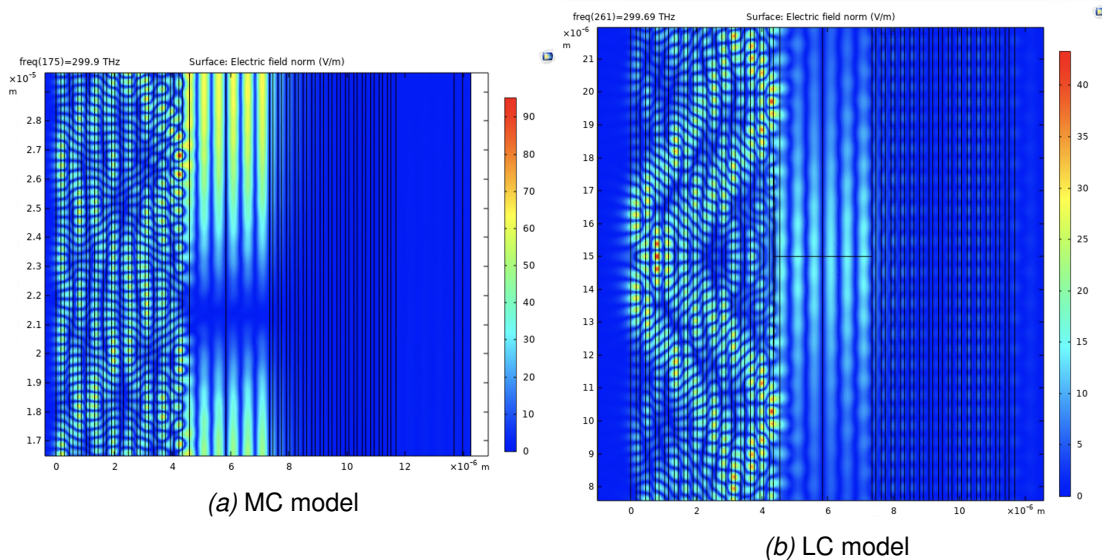


Figure 4.14. Similar electric field distributions at smaller transmission peaks in the models

The wavelength depicted in the MC model is 999.626 nm and in the LC it is 1000.348 nm . Throughout the course of this project it was unfortunately not possible to find a reasonable explanation for these distributions, but given they occurred in both models for two different curvatures there appears to be a pattern. These plots could just be a consequence of numerical errors in the simulation or a result of the boundary conditions in the simulation software. Another possible explanation is that these distributions correspond to actual physical modes inside the cavity. Learning more about them will give more insight into the simulation software or the physics it attempts to model.

4.2.3 Rayleigh length of Gaussian beams

The concept of the Rayleigh length z_0 was discussed in subsection 2.2. The key idea is that for distances from the focal place smaller than the Rayleigh length the beam waist radius can be approximated as constant. So if a laser beam is treated as Gaussian, this quantity gives a metric for the focus of the laser. In all numerical models discussed thus far the beam waist radius was defined as follows:

$$\omega_0 = \frac{20\pi}{k}$$

k is the wavevector. This is a somewhat standard setting in COMSOL and initially not much thought was given to it. If this rayleigh length is calculated for the reference frequency $\lambda_{\text{ref}} = 1000\text{nm}$ used in the models:

$$z_0 = \frac{k \omega_0^2}{2} = \frac{20^2 \pi^2}{2k} = \frac{20^2 \lambda \pi}{2} \approx 3 * 10^{-4} \text{m} = 300\mu\text{m}$$

Given that the entire setup is only $16\mu\text{m}$ wide it is safe to approximate a constant beam waist radius of the Gaussian beam when entering the cavity for all wavelengths analysed in this project.

In order to investigate the dependence of the electric field distribution on the Rayleigh length the beam waist radius was tuned so that $z_0 \approx 10^{-6}$. This way the Rayleigh length would be on the length-scale of the cavity. Moreover the beam waist radius could no longer be treated as constant. Plotting this electric field distribution for the reference wavelength λ_{ref} across the cavity yielded an electric field distribution which can be seen in Figure 4.15.

Even through increasing the incoming electric field amplitude to $|E_0| = 100\text{V/m}$ ($|E_0| = 1\text{V/m}$ in all other models) the incoming Gaussian beam is not able to significantly penetrate into the DBR cavity. It was thus concluded that the models are only very weakly dependent on the Rayleigh length, unless it is changed so drastically that the entire shape of the beam changes. The Figure 4.15 resembles very nicely the Figure 2.1. The focal plane of the Gaussian beam used in this simulation was the boundary so only the left half Figure 2.1 can be seen in Figure 4.15.

This investigation was not directly relevant for the analysis of zero dimensional cavities, but rather to test a setting in the software. However, when using the models from this project to design an actual lab experiment changing the Rayleigh length could be used to investigate optimal settings for the focus of the incoming laser beam.

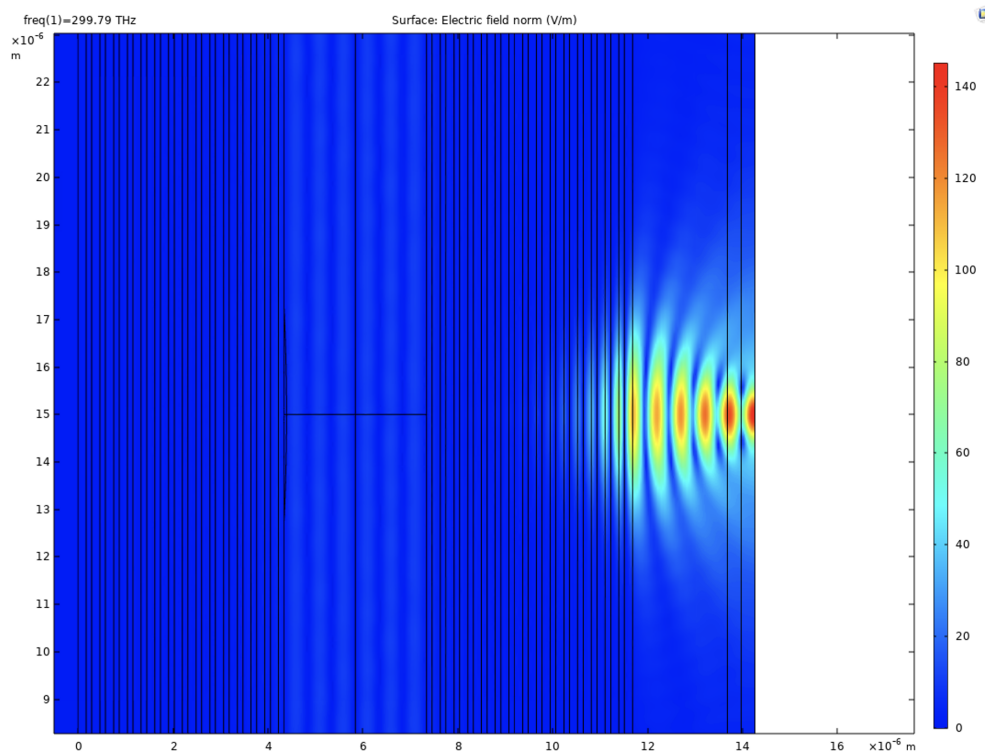


Figure 4.15. Electric field distribution across cavity for a Rayleigh length of $z_0 = 10^{-6}$ and electric field amplitude of $100V/m$

4.3 Zero dimensional DBR cavities with multiple hBN lenses

The work done by Lassaline and collaborators [27], who researched hBN lenses inside optical micro-cavities were mainly focused on a new procedure to create freeform hBN landscapes on microscopical scales. An early goal of this project has thus been to lay the foundation for numerical models, which can simulate arbitrary hBN structures inside planar Fabry-Pérot cavities. The starting point for arbitrary structures in this project was to introduce multiple lenses into the cavity. Two models were build one with two the other with four hBN lenses. In both of these the lens from the model in subsection 4.2.1 with $circ_radius = 50\mu m$ was used.

4.3.1 Two lens Model

In order to better understand arbitrary hBN shapes placed inside plane parallel Fabry-Pérot cavities a key first stepping stone would be to investigate the interference of two hBN lenses.

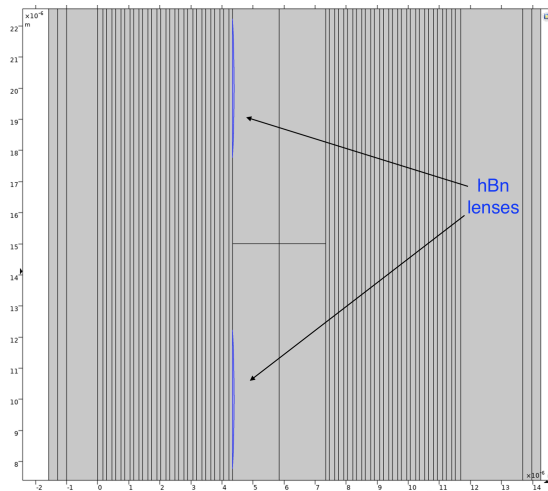


Figure 4.16. The hBN lenses highlighted in blue are each vertically displaced $5\mu m$ from the center

The two hBN lenses are identically defined to the lens in section 4.2.1 with $circ_radius = 50\mu m$ and $d_lens = 50nm$. The two lenses were located at the vertical distances $(-5\mu m, 5\mu m)$ with respect to the center of the cavity. Figure 4.16 illustrates this geometry.

Through analysing the transmission spectrum it was founds that the peak of $T = 0.932$ occurred at $1000.291nm$. From this data the Full Width Half Maximum $FWHM = 0.00228nm$ and Q-factor could be calculated.

$$Q_{2\ lens} = \frac{1000.291nm}{0.00228nm} = 438172 \approx 438000$$

4 Results

The Q-factor is again very similar to the one in the original model in subsection 4.2.1 reinforcing the point that this quantity does not seem to depend significantly on the hBN lenses. Now considering the electric field distribution at the resonance frequency.

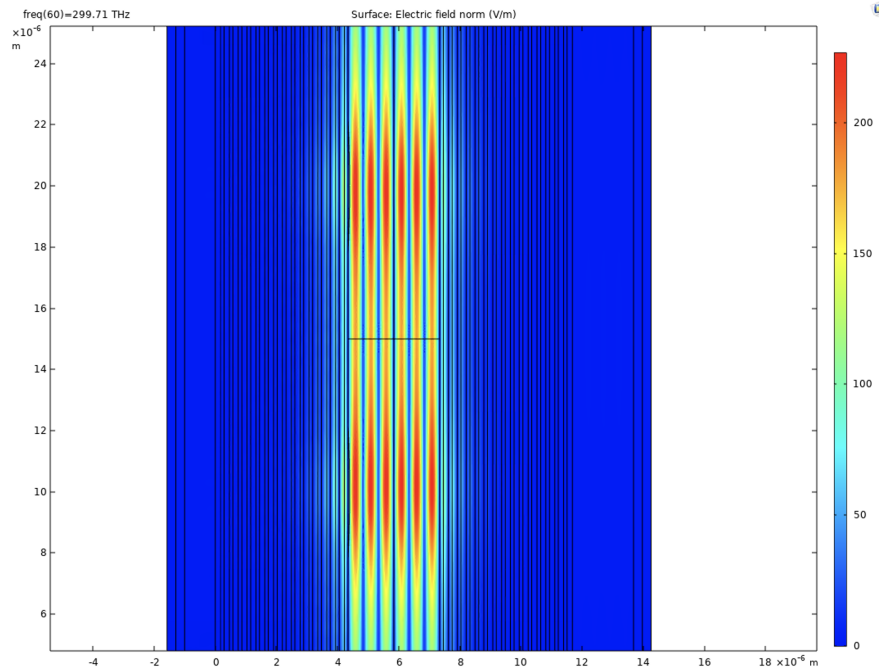


Figure 4.17. Electric field distribution across cavity in two lens model at the resonance frequency

In Figure 4.17 it can be seen that largest electric field norms can be found in front of the lenses. A more nuanced analysis of the plot shows that the peak electric field norm has decreased with respect to the distribution of one hBN lens in Figure 4.6. Moreover, the electric field norm in front of the lenses in the vertical direction falls off much less on the side closer to the other lens. There is some positive interference between the two cavities in the center of the cavity. In order to better analyse the interference of the two lenses in the transverse plane a vertical line cut was taken at the first of the six longitudinal peaks. This cut is depicted in Figure 4.18.

The vertical line cut in Figure 4.18 shows that the electric field in the transverse plane is concentrated in front of the two lenses. However both peaks are smaller compared to the similar plot in 4.7, which could be result of the their different location in the lens as opposed to the model in section 4.2.1. However, it is quite likely that there is some negative interference happening between the two lenses. Particularly interesting is that in Figure 4.18 it can be seen that the electric field norm falls of much less quickly from the lenses in the direction of the center. This can be explained by some positive interference of the two lenses in the center region. Another feature of this plot are the three fluctuations of the electric field norm around the center of the cavity. It would be interesting to investigate whether the fluctuations get amplified or reduced when the distance between the lenses is

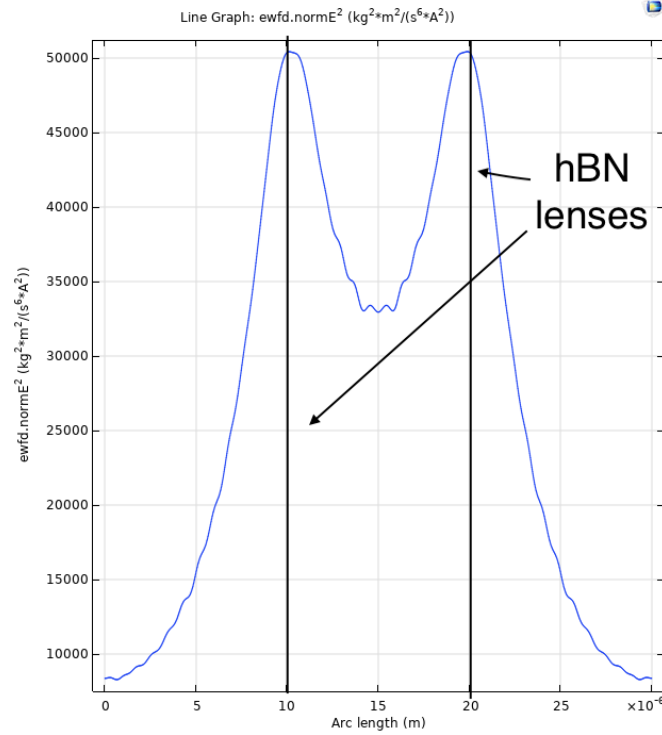


Figure 4.18. Vertical line cut of the electric field distribution squared of the two lens model

altered. A detailed study to analyse this further would consist of varying the length in small increments to see how the interference changes.

4.3.2 Four lens Model

The idea behind the four lens model was to place the lenses very close to each in order to observe the interference. For this the original model in subsection 4.2.1 was used in which four identical copies of the $circ_radius = 50\mu m$ lens were made. The lenses were arranged as shown in Figure 4.19.

The separation of $4.4\mu m$ was chosen so that the overlap between lenses was fairly small. The four lenses were located at the vertical distances $(-6.6\mu m, -2.2\mu m, 2.2\mu m, 6.6\mu m)$ with respect to the center of the cavity.

Again the transmission spectrum around the reference wavelength was examined to find a transmission peak of $T = 0.92$ was located at $1000.581nm$. From this data the Full Width Half Maximum $FWHM = 0.00671nm$ and the Q-factor could also be calculated.

$$Q_{4 \text{ lens}} = \frac{1000.581nm}{0.00671nm} = 149078 \approx 149\,000$$

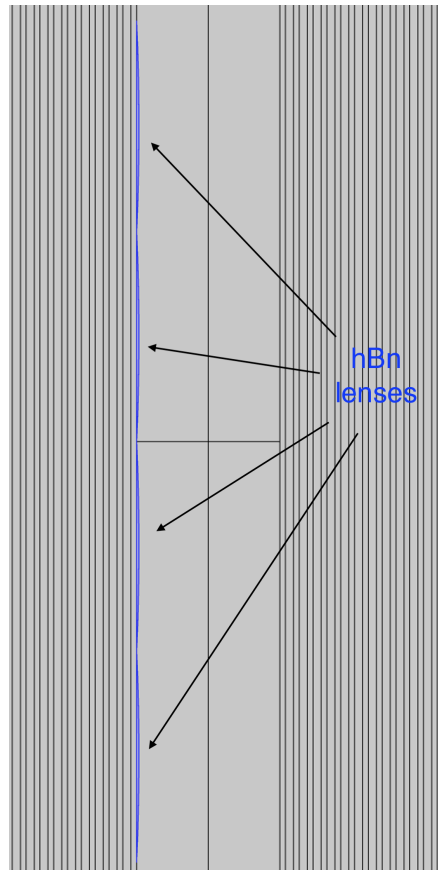


Figure 4.19. The four identical lenses were placed inside the cavity at a separation of $4.4\mu m$

This is rather surprising as the Q-factor in the four lens model at the fundamental resonance peak is the first one that is significantly different from all the other models. The 'wall' of hBN created by the slightly overlapping four lenses appears let photons escape much more easily.

The electric field distribution of the four lens model at resonance frequency is given by Figure 4.20.

This distribution looks a little bit similar to what could be seen in the one lens model in Figure 4.6. The peak electric field amplitude is smaller by about $60V/m$. Especially the sinusoidal nature of the longitudinal distribution is shared by both plots. A key difference is that the area where the electric field norm is concentrated is much more spread out than in the one lens model. Another similarity can be drawn to the two lens model in Figure 4.17 with respect to the positive interference in the center. Interestingly there appears to be negative interference in front of the two lenses not adjacent to the center. This is in contrast to the electric field distribution seen with two lenses in 4.17, where the electric field was concentrated in front of both lenses. It is quite likely that the separation of the lenses plays a key role in this process. Investigating the conditions under which the electric field

4 Results

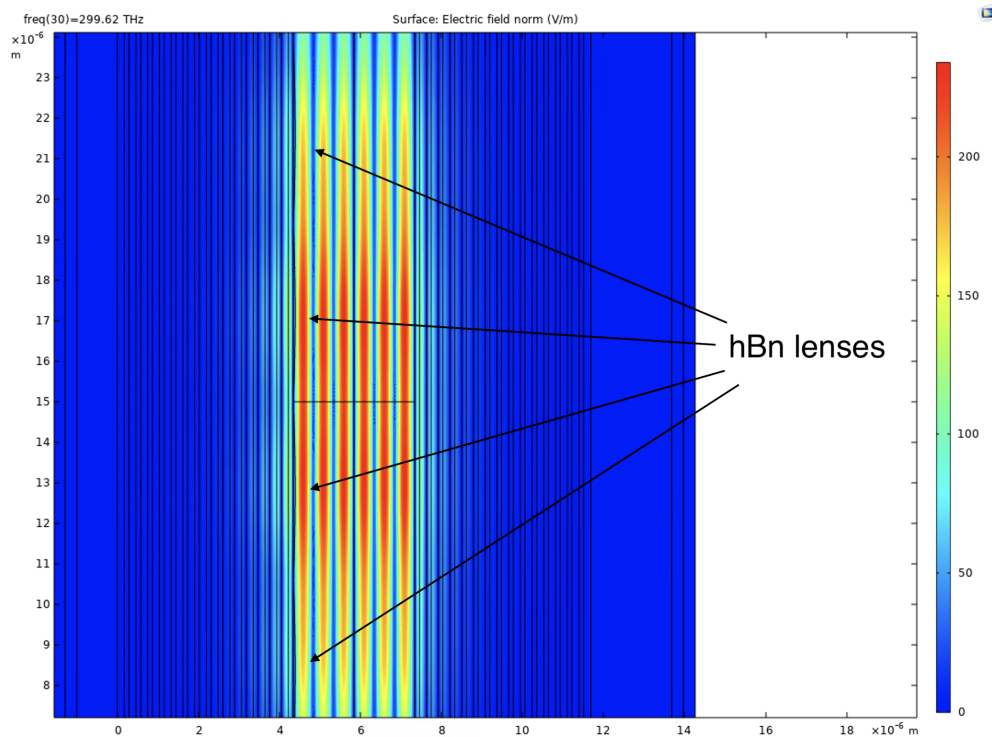


Figure 4.20. Electric field distribution of the four lens model at the resonance frequency

concentrates in front of a given lens in a multi-lens system is definitely worth investigating further. The dependence of this on the number of lenses would also be an intriguing study. A good first step in such an analysis could be to build a model with six lenses and see how the electric field distribution changes.

5 Conclusion and Outlook

This project consisted of building numerical simulations of hBN lens zero-dimensional Fabry-Pérot cavities in COMSOL Multiphysics[®]. It was shown that this software can be used to replicate existing models of plane-parallel Fabry-Pérot cavities such as the TMM python library. The simulations were also able to show the existence of the fundamental Gaussian mode through the introduction of an hBN lens, which was measured experimentally. As the field of introducing freeform hBN structures into Fabry-Pérot cavities is relatively new not a lot of experimental or theoretical research was available to support the validity of the other models used in this project. The simulations build over the course of this project should serve as a stepping stone for research in this field. A number of interesting features of hBN lenses inside Fabry-Pérot cavities could be identified. Smaller transmission peaks showed some periodic nature in the transverse confinement. The analysis done in this project showed some interesting results, with regards the electric field distribution inside the cavity and its dependence on the curvature on the lens. The data suggested that more curved lenses lead to resonance peaks at higher wavelengths. Moreover, the curvature of the lens also impacted the peak electric field distributions. Introducing multiple lenses to the system yielded some intriguing findings about the interference between the lenses. Especially the oscillatory nature of the electric field distribution near the center of the cavity is worth investigating further. Moreover, through investigating a model with four hBN lenses it could be seen that the electric field only concentrates on some of them.

A main limitation of the numerical tools used in this analysis was the frequency sweep done in the COMSOL Multiphysics[®] software. In this analysis it is quite likely that a few interesting features of the models were missed by chance because the frequency sweep missed them. Examples of this likely include higher order transverse Gaussian modes and other transmission peaks of similar height as the fundamental mode. Future investigations could improve on this through increasing the computational scope of the simulations.

The models developed over the course of this project are meant as a starting ground for further numerical analysis of these types of systems. This work barely scratches the surface of the physics to be done with hBN lens zero-dimensional Fabry-Pérot cavities. A number of interesting questions are open after this analysis, such as the dependence of the peak electric field norm on the curvature, the higher order Gaussian modes and the

interference mechanism of multiple lenses inside the cavity. Throughout the entire project the absorption of all materials was assumed negligible. Future models could include a nonzero absorption coefficient in order to describe the physical situation more accurately. Newer simulations may also be concerned with investigating the dependence of the electric field distribution on the separation of the DBR mirrors, which would give some more insight into the longitudinal confinement of the system. This is difficult to do with the models developed in this project as the entire model needs to be recomputed if the geometry is changed. Moreover, newer models developed within COMSOL physics could be concerned with implementing the geometries discussed in this project in three dimensional models. This way higher order Gaussian modes might become visible as well.

Bibliography

- [1] Mohammad H. Bitarafan and Ray G. DeCorby. “On-Chip High-Finesse Fabry-Perot Microcavities for Optical Sensing and Quantum Information”. In: *Sensors* 17.8 (2017). ISSN: 1424-8220. URL: <https://www.mdpi.com/1424-8220/17/8/1748>.
- [2] Stefan Bogdanovic. “Diamond-based Fabry-Perot microcavities for quantum networks”. en. Doctoral Thesis. Delft, 2017. URL: <https://doi.org/10.4233/uuid:29c23e60-9f4c-4d5e-9ab9-9bf6c520df01>.
- [3] Steven J. Byrnes. *Multilayer optical calculations*. 2020. arXiv: 1603.02720 [physics.comp-ph].
- [4] Iacopo Carusotto and Cristiano Ciuti. “Quantum fluids of light”. In: *Reviews of Modern Physics* 85.1 (Feb. 2013), pp. 299–366. ISSN: 1539-0756. DOI: 10.1103/revmodphys.85.299. URL: <http://dx.doi.org/10.1103/RevModPhys.85.299>.
- [5] James Clerk Maxwell. “A dynamical theory of the electromagnetic field [abstract only]”. In: 13 (???? 1864), pp. 531–531. ISSN: 0370-1662 (print), 2053-9126 (electronic).
- [6] COMSOL. *Comsol Multiphysics User Guide*. English. Version Version 4.3. COMSOL Inc. 2012. 1292 pp. December 16, 2012.
- [7] COMSOL. *Fabry-Perot Cavity*. en. 2021. URL: <https://www.comsol.com/model/fabry-perot-cavity-14711> (visited on 12/30/2021).
- [8] COMSOL. *Ray Optics Module*. en. 2021. URL: <https://www.comsol.ch/ray-optics-module> (visited on 12/29/2021).
- [9] COMSOL. *Wave Optics Module*. en. 2021. URL: <https://www.comsol.ch/wave-optics-module> (visited on 12/29/2021).
- [10] DrBob. *The transmission of an etalon as a function of wavelength. A high-finesse etalon (red line) shows sharper peaks and lower transmission minima than a low-finesse etalon (blue)*. en. 2021. URL: https://en.wikipedia.org/wiki/Fabry%E2%80%93Perot_interferometer#/media/File:Etalon-2.png (visited on 01/02/2022).
- [11] Paul Eastham. “Nanophotonics I: quantum theory of microcavities”. en. Dublin, 2016. URL: <https://www.tcd.ie/Physics/people/Paul.Eastham/nanophotonics.pdf>.

- [12] Mark A. Finlayson. *Wave Optics Module User's Guide*. English. Version Version 5.4. COMSOL Inc. 2020. 180 pp. December 16, 2021.
- [13] Enrique J. Galvez. "Gaussian Beams". en. Madison County, 2014. URL: https://www.google.com/url?sa=t&rct=j&q=&esrc=s&source=web&cd=&ved=2ahUKEwj75o2dwYL1AhU_iv0HHUfCAeQQFnoECBQQAQ&url=http%3A%2F%2Fwww.colgate.edu%2Fportaldata%2Fimagegallerywww%2F98c178dc-7e5b-4a04-b0a1-a73abf7f13d5%2Fimagegallery%2Fgaussian-beams.pdf&usg=AOvVaw0NXulXRy-foPCK0ilUeENI.
- [14] Stephan Giglberger. "Anleitung zum Anfängerpraktikum B Versuch „fp“: Fabry-Perot-Interferometer". en. Regensburg, 2010. URL: <https://www.uni-regensburg.de/assets/physik/praktika/B/fp.pdf>.
- [15] Marco Buchmann H.M. Singer Lorenz Müller. "Introduction to Computational Physics0". en. Zurich, 2010. URL: https://ethz.ch/content/dam/ethz/special-interest/baug/ifb/ifb-dam/homepage-IfB/Education/bsc_courses/bsc-intro-comphys/documents/CompPhysScript-2017.pdf.
- [16] Eugene Hecht. *Optics, 5th Edition*. en. Pearson, 2017, pp. 625–626. ISBN: 978-1-292-09693-3.
- [17] Eugene Hecht. *Optics, 5th Edition*. en. Pearson, 2017, pp. 436–440. ISBN: 978-1-292-09693-3.
- [18] R. Hiptmair. "Numerical Methods for Partial Differential Equations". en. Zurich, 2016. URL: <https://people.math.ethz.ch/~hiptmair/tmp/NPDE/NPDE16.pdf>.
- [19] Lucas Hofer. *M² and High-order Modes*. en. 2016. URL: <https://dataray.com/blogs/dataray-blog/m-sup2-and-high-order-modes> (visited on 12/26/2021).
- [20] Christina Hood. "Real-time measurement and trapping of single Atoms by single Photons". en. Doctoral Thesis. Pasadena, 2000. URL: https://thesis.library.caltech.edu/3688/1/Hood_cj_2000.pdf.
- [21] Christian Huber. "Micromechanical tunable Fabry-Perot interferometers with membrane Bragg mirrors based on silicon/silicon carbonitride". en. Doctoral Thesis. Karlsruhe, 2019.
- [22] John D. Joannopoulos et al. *Photonic Crystals: Molding the Flow of Light (Second Edition)*. 2nd ed. Princeton University Press, 2008. ISBN: 0691124566. URL: <http://ab-initio.mit.edu/book/photonic-crystals-book.pdf>.
- [23] Joseph Buck Jr. "Cavity QED in Microsphere and Fabry-Perot Cavities". en. Doctoral Thesis. Pasadena, 2003. URL: <https://core.ac.uk/download/pdf/11811245.pdf>.
- [24] Michael Ware Justin Peatross. *Physics of Light and Optics*. en. Pearson, 2021. ISBN: 978-1-312-92927-2.

- [25] Ursula Keller. *Ultrafast Lasers*. en. Zürich: Springer International Publishing, 2021.
- [26] Uday Kiran Khankhoje. "PHOTON CONFINEMENT IN PHOTONIC CRYSTAL CAVITIES". en. Doctoral Thesis. Pasadena, 2010. URL: <https://thesis.library.caltech.edu/5873/1/thesis-uday-full.pdf>.
- [27] Nolan Lassaline et al. "Freeform Electronic and Photonic Landscapes in Hexagonal Boron Nitride". In: *Nano Letters* 21.19 (2021). PMID: 34591490, pp. 8175–8181. DOI: 10.1021/acs.nanolett.1c02625. eprint: <https://doi.org/10.1021/acs.nanolett.1c02625>. URL: <https://doi.org/10.1021/acs.nanolett.1c02625>.
- [28] Bert Novotny Lukas; Hecht. *Principles OF Nano-Optics*. en. Cambridge University Press, 2012. ISBN: 9780511794193.
- [29] Lukas Novotny. *Lecture Notes on Electromagnetic Fields and Waves*. en. 2019.
- [30] Rüdiger Paschotta. *Optical Intensity*. en. Oct. 10, 2020. URL: https://www.rp-photonics.com/optical_intensity.html (visited on 12/26/2021).
- [31] Rüdiger Paschotta. *Q Factor*. en. 2020. URL: https://www.rp-photonics.com/q_factor.html (visited on 12/29/2021).
- [32] Mikhail Polyanskiy. *Optical constants of BN (Boron nitride)*. en. 2022. URL: <https://refractiveindex.info/?shelf=main&book=BN&page=Lee> (visited on 01/01/2022).
- [33] Renato Renner. "Elektrodynamik". de. Zurich, 2010. URL: <https://edu.itp.phys.ethz.ch/fs10/ed/skript.pdf>.
- [34] Alaa Sharhan. "Transfer Matrix Mathematical Method for Evaluation the DBR Mirror for Light Emitting Diode and Laser". In: *Journal of Physics: Conference Series* 1535 (May 2020), p. 012018. DOI: 10.1088/1742-6596/1535/1/012018.
- [35] S. Sukudlarek. "The simulation of a plane-concave Fabry-Perot micro-cavity". en. Bachelor's Thesis. Leiden, 2019.
- [36] Andrzej Wolski. *Theory of Electromagnetic Fields*. en. 2011. URL: [arXiv:1111.4354](https://arxiv.org/abs/1111.4354) (visited on 12/26/2021).
- [37] Erich Zauderer. "Complex argument Hermite-Gaussian and Laguerre-Gaussian beams". en. In: *Journal of the Optical Society of America* 3.4 (1986), pp. 465–469.

List of Figures

2.1	Illustration of a Gaussian Beam [28]	8
2.2	A few higher order Laguerre-Gaussian modes [19]	10
2.3	A single beam entering the system creates interference of many beams [14]	11
2.4	Illustration of the Airy function $\mathcal{A}(\theta)$, which plots the ratio of the transmitted intensity I_t to the incident intensity I_i in relation to the phaseshift δ [17]	15
2.5	Transmission plot of a Fabry-Pérot cavity where the Free Spectral Range, Full Width Half Maximum and Finesse are shown [10]	18
2.6	Illustration of a distributed Bragg reflector with a quarter wavelength separation of the layers [24]	18
2.7	A simplified model of a multi-layer stack with N layers where each layer i has refractive index n_i and thickness d_i .	19
2.8	Simulation of distributed Bragg reflector of a typical Reflectance vs. Wavelength plot done using the Python TMM library. This plot describes a DBR with 15 Bragg pairs where the refractive indices 2.91 and 3.45 corresponding to the material AlAs and GaAs respectively were used	21
2.9	Illustration of a planar-concave Fabry-Pérot cavity where the second mirror M_2 is curved. The beam waist of a Gaussian mode is then drawn in blue to highlight the confinement of the photons underneath the dimple [2]	25
2.10	An illustration of an hBN lens inside the Fabry-Pérot micro-cavity. Marked in red is the concentrated electric field which can be seen to concentrate on top of the lens [27]	26
3.1	A simple example of meshing a rectangle geometry within COMSOL	28
3.2	A list of all the model parameters	29
3.3	The geometry of a 2D DBR Fabry-Pérot cavity in COMSOL as well its boundary conditions are depicted	31
3.4	"The perfect electric conductor boundary condition is used on exterior and interior boundaries representing the surface of a lossless metallic conductor or (on exterior boundaries) representing a symmetry cut. The shaded (metallic) region is not part of the model but still carries effective mirror images of the sources. Note also that any current flowing into the boundary is perfectly balanced by induced surface currents. The tangential electric field vanishes at the boundary." [12]	33

3.5	"The perfect magnetic conductor boundary condition is used on exterior boundaries representing the surface of a high impedance region or a symmetry cut. The shaded (high impedance) region is not part of the model but nevertheless carries effective mirror images of the sources. Note also that any electric current flowing into the boundary is forbidden as it cannot be balanced by induced electric surface currents. The tangential magnetic field vanishes at the boundary. On interior boundaries, the perfect magnetic conductor boundary condition literally sets the tangential magnetic field to zero which in addition to setting the surface current density to zero also makes the tangential electric field (and in dynamics the tangential electric field) discontinuous" [12]	34
3.6	Examples of the meshing inside the geometry	35
4.1	Data overlay of the COMSOL and TMM python models	38
4.2	The electric field distribution is plotted at the resonance frequency of the cavity. This frequency is the peak in the transmission spectrum	40
4.3	The lens is created by intersecting the circle and the rectangle	41
4.4	The first hBN lens in the Geometry	42
4.5	Transmission spectrum for one hBN lens with $circ_radius = 50\mu m$	43
4.6	Distribution of the electric field norm at the resonance frequency of the zero dimensional Fabry-Pérot cavity with one hBN lens at $circ_radius = 50\mu m$	43
4.7	A vertical line cut of the electric field distribution squared across the entire cavity shows the fundamental (0,0) Gaussian mode	44
4.8	Zoomed in Transmission Plot to highlight the second peak.	45
4.9	Electric field distribution of a second transmission peak located at $998.254nm$	46
4.10	Vertical lines cuts of the electric field distribution squared at a second smaller resonance peak	47
4.11	The three differently curved hBN lenses (blue) depicted inside their respective geometry	48
4.12	Electric field distributions of both models at the resonance frequency	50
4.13	Vertical line cuts in the electric field distributions squared of both models at the resonance frequency	50
4.14	Similar electric field distributions at smaller transmission peaks in the models	51
4.15	Electric field distribution across cavity for a Rayleigh length of $z_0 = 10^{-6}$ and electric field amplitude of $100V/m$	53
4.16	The hBN lenses highlighted in blue are each vertically displaced $5\mu m$ from the center	54
4.17	Electric field distribution across cavity in two lens model at the resonance frequency	55
4.18	Vertical line cut of the electric field distribution squared of the two lens model	56

4.19 The four identical lenses were placed inside the cavity at a separation of $4.4\mu m$	57
4.20 Electric field distribution of the four lens model at the resonance frequency .	58

Appendices

A Appendix: Python code

Below is the python code used to model the planar Fabry-Pérot cavities with the TMM library. This code served as the tool for verification of the early models in this project. This code was greatly inspired by a code written for the *Optical Properties of Semiconductors* class at ETH Zurich in the Autumn Semester of 2021.

```
1 import numpy as np
2 import matplotlib.pyplot as plt
3 %matplotlib notebook
4 ##matplotlib inline
5 from scipy.interpolate import interp1d
6 import tmm
7
8 def gen_dbr(n1, n2, wl, pairs, odd=False):
9     #Create pile of lambda/4 layers of refractive indices n1 and n2
10    n, d = [], []
11    for i in range(pairs):
12        n.extend((n1, n2))
13        d.extend((wl/4/n1, wl/4/n2))
14    if odd:
15        n.append(n1)
16        d.append(wl/4/n1)
17    return n, d
18
19 n_SiO2 = 1.4570
20 n-Ta2O5 = 2.1205
21 n_air = 1
22 wavelength = 1000
23 d_mirrors = 3000
24 stack_n, stack_d = gen_dbr( n_SiO2, n-Ta2O5, wavelength,
```

```

25                                     15, odd=False)
26
27 # Layer thicknesses (nm):
28 d = [np.inf, *stack_d, d_mirrors, *stack_d[::-1], np.inf]
29 # Layer refractive indices:
30 n = [n_air, *stack_n, n_air, *stack_n[::-1], n_air]
31 thetas = np.linspace(0, np.pi/2, 15001)
32 Rs = np.zeros(thetas.shape)
33 Rp = np.zeros(thetas.shape)
34 Ts = np.zeros(thetas.shape)
35 Tp = np.zeros(thetas.shape)
36 for i, theta in enumerate(thetas):
37     s = tmm.coh_tmm('s', n, d, theta, wavelength)
38     Rs[i] = s['R']
39     Ts[i] = s['T']
40     p = tmm.coh_tmm('p', n, d, theta, wavelength)
41     Rp[i] = p['R']
42     Tp[i] = p['T']
43
44 # Assuming no dispersion for simplicity...
45 theta = 0
46 wavelengths = np.linspace(800, 1150, 15001)
47 Rs_wl = np.zeros(wavelengths.shape)
48 Rp_wl = np.zeros(wavelengths.shape)
49 Ts_wl = np.zeros(wavelengths.shape)
50 Tp_wl = np.zeros(wavelengths.shape)
51
52 for i, wl in enumerate(wavelengths):
53     s = tmm.coh_tmm('s', n, d, theta, wl)
54     Rs_wl[i] = s['R']
55     Ts_wl[i] = s['T']
56     p = tmm.coh_tmm('p', n, d, theta, wl)
57     Rp_wl[i] = p['R']
58     Tp_wl[i] = s['T']
59 s = tmm.coh_tmm('s', n, d, theta, wavelength)
60
61
62 f, ax = plt.subplots(1, 1, figsize=(6, 4))
63 ax.set_xlabel(r'Wavelength_(nm)')
64 ax.set_xlim(wavelengths.min(), wavelengths.max())

```

```

65 ax.plot(wavelengths, Ts_wl, label=r'$T_s$')
66 ax.plot(wavelengths, Tp_wl, label=r'$T_p$', ls='-')
67 ax.legend()
68 ax.set_title('DBR_Fabry_Perot_Cavity_Transmission_')
69 f.tight_layout()
70
71
72
73 #import textfile and convert it to string
74 lines = []
75 with open('30_12_planeW_plot_trans_peak.txt') as f:
76     lines = f.readlines()
77
78 #create numpy array out of it
79 temp = np.array(lines)
80
81 #build new array to work with
82 temp2 = temp
83 for i in range(8):
84     temp2 = np.delete(temp2, 0)
85
86 #group the numbers together in new array
87 t3 = []
88 t3.append("")
89 numcount = 0
90 for j in temp2:
91     t2 = j
92     for i in t2:
93         if(i != '_' and i != "\n"):
94             t3[numcount] += i
95         if(i == '_' and i != "\n"):
96             t3.append("")
97
98             numcount+=1
99     t3.append("")
100     numcount+=1
101
102 #convert array of strings to array of floats
103 t4 = []
104 for index, string in enumerate(t3):

```



```

105     if(string != ''):
106         t4.append(float(t3[index]))
107
108 #split array of floats into two arrays, one for wavelengths
109 #the other for the corresponding T-coefficients
110 wavelengths2 = []
111 trans = []
112 wave = True
113 for i in t4:
114     if(wave):
115         wavelengths2.append(i)
116     else:
117         trans.append(i)
118     wave = not wave
119
120 #plot result on top of theoretical calculations
121 f, ax = plt.subplots()
122
123 ax.set_xlabel(r'Wavelength_(nm)')
124 ax.set_xlim(wavelengths.min(), wavelengths.max())
125 ax.plot(wavelengths, Ts_wl, label=r'$T_s$')
126 ax.plot(wavelengths, Tp_wl, label=r'$T_p$', ls='--')
127 ax.plot(wavelengths2, trans, label=r'COMSOL')
128 ax.legend()
129 ax.set_title('Fabry_Perot_cavity_with_incident_plane_Wave')
130 plt.tight_layout(pad=2)

```